

# Fourier Series based Analytic Model of a Resonant MEMS Mirror for General Voltage Inputs

Han Woong Yoo *Member, IEEE*, Stephan Albert, Georg Schitter *Senior Member, IEEE*,

**Abstract**—This paper proposes an analytic model of a resonant MEMS mirror with electrostatic actuation based on a Fourier series approximation for both the comb drive torque and the input waveform and verifies the model by measurements using rectangular input waveforms with various duty cycles. The analytic model is derived by the perturbation method, results in slow flow evolution in amplitude and phase with dynamic influence matrices and vectors and also provides the local dynamics for each equilibrium described by a Jacobian matrix. An analysis of the dynamic influence matrices and vectors provides understanding of the mirror dynamics by frequency components of the input waveform and the comb drive capacitance. The asymptotic behavior at zero amplitude provides the transition curve in an extended dynamic model, which corresponds to the well-known Mathieu's equation solely with the constant and fundamental frequency components of the input waveform. The measurement results verify the proposed model, showing less than  $\pm 0.06$  % frequency error for large amplitudes and  $\pm 0.47$  % for small amplitudes, which corresponds to  $\pm 1.2$  Hz and  $\pm 9.6$  Hz for the case of a mirror with 2 kHz natural frequency, respectively. Measurements of local dynamics and transition curves also show a good agreement with the proposed model, which can be used for a fast and accurate analysis of resonant MEMS mirrors for high precision applications.

**Index Terms**—MEMS Mirror, Parametric Resonance, Duffing Equation, Perturbation Theory, Discrete Fourier Transform, Bessel Function, General Input Waveform, Transition Curve, Automotive Lidar

## I. INTRODUCTION

RESONANT MEMS mirrors are promising candidates as beam-steering solution for wide angles at high frequencies in various applications, such as laser scanning displays [1], [2], scanning laser microscopy [3], [4], and automotive lidars [5]–[9]. Bulk-micromachined scanners equipped with electrostatic actuation, specifically with out-of-plane comb drives, form a frequent subclass of resonant MEMS mirrors, because of fabrication compatibility, long-term stability, integratability into the full scan system, competitive unit price by large volume production, and well distributed driving force along the large scan displacement [2]. However, such electrostatically actuated resonant MEMS mirrors typically operate in parametric resonance, exhibiting various nonlinear effects e.g. the occurrence of driven oscillations confined to

discrete frequency regions [10], [11] and bifurcations [12]–[14]. These nonlinearities add difficulties in a fast and accurate analysis of the dynamics for design and control purposes of such MEMS mirrors, especially for demanding applications that require high precision and robustness, e.g. MEMS lidars [15].

To analyze the impacts of such nonlinearities, various models have been proposed. The nonlinear torque function of comb drives has been modeled by polynomial functions [11], [13], [16]–[19], rational or hyperbolic functions [20]–[22], piecewise functions [23], Gaussian functions [24], [25], and Fourier series [26]. The model is desired to describe and explain the dynamics accurately at all amplitudes to understand the dynamical behavior in order to optimize the performance in application use. For automotive lidars, for example, an accurate model of MEMS resonant mirrors at large amplitudes is important to understand robustness properties against harsh environment conditions, such as wide ranges of temperature, pressure and vibration [15], [27], [28]. Instability conditions at zero amplitude are also crucial since they influence the fast start-up of the MEMS scan system after a sudden failure [29], [30]. However most aforementioned models with an out-of-plane comb drive torque show high accuracy only at either small or large amplitudes mainly due to approximation errors.

Beside the comb drive models, voltage inputs to the comb drives are also relevant for the analysis of the response behavior. A square rooted sine waveform is popular in analysis because it results in a single tone harmonic input at small amplitudes, leading to the well-known Mathieu equation [11], [13], [18], [19]. In practice, rectangular voltage inputs are widely used due to their maximized energy injection into the oscillation and simplicity in implementation, leading to optimized actuator dimensions and reduced power consumption of the driving circuitry [31], [32]. The rectangular voltage inputs are also beneficial for the control of both amplitude and phase at the same time, by either leveling of the voltage source or digitally changing the on-off switching timing [13], [30], [33]–[35]. Generally, Fourier decomposition has been used in the case of general inputs for instability analyses of Hill equations and forced Duffing oscillators since it represents an extension of single tone analysis and also allows to apply Floquet theory directly [36]–[40]. For MEMS mirrors with out-of-plane comb drive actuators, rectangular voltage inputs are analyzed by Fourier decomposition with various duty cycles, leading to an instability analysis by the Lindstedt-Poincaré technique [24], which is applied for a vertical scanning actuator [25]. A Fourier series based analytic model of parametrically driven MEMS mirrors with out-of-plane comb drive actuators is

This work has been supported in part by the Austrian Research Promotion Agency (FFG) under the scope of the LiDeAR project (FFG project number 860819). Han Woong Yoo and Georg Schitter are with Automation and Control Institute (ACIN), TU Wien, Gusshausstrasse 27-29, 1040 Vienna, Austria, and Stephan Albert is with Infineon Technologies AG, Am Campeon 1-15, 85579, Neubiberg, Germany. (corresponding author: Han Woong Yoo; phone: +43 1 58801 376518; e-mail: yoo@acin.tuwien.ac.at) This article has supplementary downloadable material available. Digital Object Identifier: 10.21227/5d70-mg50

proposed for a square rooted sine voltage input and shows a high accuracy at large amplitudes [26]. For general voltage inputs, however, there is no analytic model yet that accurately describes the actual behavior of the mirror over its full amplitude range.

The main contribution of this paper is an accurate analytic model of global as well as local dynamics of a parametrically driven resonant MEMS mirror with general voltage inputs. Additionally, the model extends its high accuracy to small amplitudes by a compensated torque approximation and an asymptotic slow flow model at zero amplitude. The measured angular derivative of the comb drive capacitance is sharpened near zero angle, which compensates for distortions caused by the limited bandwidth of the sensing circuitry. Both the voltage inputs and the angular derivative of the comb drive capacitance are modeled by a finite set of analytic functions in two Fourier series. By averaging over an oscillation period, slow flow dynamics of amplitude and phase are derived using dynamic influence matrices and vectors given by Bessel functions depending on the mirror amplitude. Asymptotic behavior at zero amplitude provides phase equilibria, which are related to the start-up behavior of the parametric resonance. The proposed slow flow model provides an accurate approximation of the global and the local dynamics for both high amplitudes in nominal operation and small amplitudes for start-up. In addition, the proposed model is computationally efficient, allowing additional analysis of stationary solutions and bifurcations readily.

The paper is organized as follows. Section II discusses a single degree of freedom (SDoF) model of the MEMS mirror and a Fourier series based approximation of the comb drive torque and the input waveform. Section III describes the slow flow dynamics and their local dynamics with dynamic influence matrices and vectors and further analyzes the structure of the dynamic influence matrices and the asymptotic behavior at zero amplitude. In Section IV, the proposed models are verified with the measurement data via frequency responses, transition curves, and the local dynamics using rectangular input waveforms with various duty cycles. Finally, Section V summarizes the outcome of the paper.

## II. DYNAMIC MODEL OF A MEMS MIRROR

This section describes the analytical structure chosen for the MEMS mirror dynamics, the comb drive torque, and the voltage input in the equation of motion for further analysis by perturbation theory. The MEMS mirror [26], [41] used in verification is a variant of the MEMS mirror in [14], [35] with an elliptic mirror. Fig. 1 illustrates a conceptual drawing of major features of the MEMS mirror in addition to the mirror itself, e.g. comb drives, leaf springs and torsion bars [42]. The out-of-plane electrostatic comb drives consist of inner and outer electrode rows for enhancing the torque at small angles. The leaf springs provide the dominant portion to the restoring torque, enabling high scanning frequencies, and introduce a significant geometric hardening effect. Short and narrow torsion bars efficiently suppress rigid body modes different from the intended rotational motion. A detailed discussion of

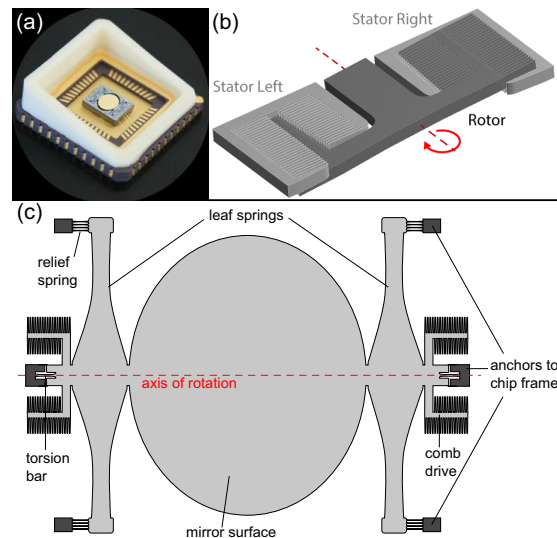


Fig. 1. (a) A photographic picture of the resonant MEMS mirror used for verification. (b) Perspective view of out-of-plane comb drive with inner and outer electrode rows. (c) Conceptual drawing of the MEMS mirror rotor used in verification. The out-of-plane electrostatic comb drive consists of two pairs of comb drive arms for each side of the elliptic mirror with a long axis of 2.7 mm. The mirror is suspended by two pairs of leaf spring suspensions and two torsion bars. The leaf springs are connected to the frame via relief springs in order to reduce geometric hardening.

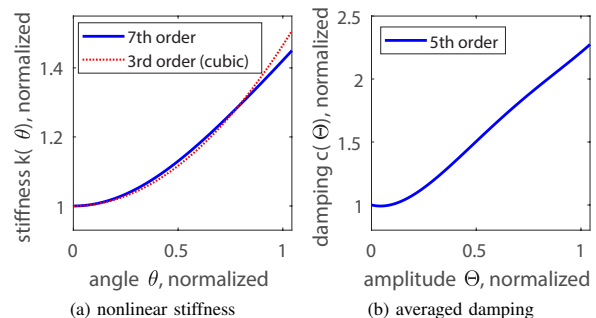


Fig. 2. Nonlinear stiffness function and averaged damping function from experimental identification. The stiffness identification using only linear and cubic terms is also drawn for comparison.

the design concepts and the parameter identification can be found in [26].

### A. Dynamic Model of Resonant MEMS Mirror

Consider a single degree of freedom (SDoF) equation of motion for the MEMS mirror angle  $\theta$  as a generalized Duffing equation [14], [43]

$$I\ddot{\theta} + c(\Theta)\dot{\theta} + k(\theta)\theta = \frac{1}{2} \frac{dC}{d\theta} V^2(t), \quad (1)$$

where  $I$  denotes the inertia of the mirror in the considered rotational mode,  $c$  denotes the averaged damping function and

$k$  denotes the nonlinear stiffness function given by

$$c(\Theta) = c_0 + c_1\Theta + c_2\Theta^2 + c_3\Theta^3 + c_4\Theta^4 + c_5\Theta^5, \quad (2)$$

$$k(\theta)\theta = k_1\theta + k_3\theta^3 + k_5\theta^5 + k_7\theta^7, \quad (3)$$

where  $c_i$  denotes the nonlinear damping coefficient of the  $i$ -th polynomial term in the amplitude  $\Theta$  [14] and  $k_i$  denotes the nonlinear stiffness coefficient of the  $i$ -th polynomial term in the angle  $\theta$ . The averaged damping function is a behavioral approximation of the damping in slow flow evolution [26]. The orders of (2) and (3) are chosen based on a prior study [14] to obtain a close fit of mechanical parameters from measurements. The nonlinear stiffness function is identified by the amplitude-frequency relation of the backbone curve [26]. By an actuated decay, i.e. the ring-down oscillation with a DC voltage applied to the comb drives, the angular derivative of the capacitance is obtained via the comb drive current measured with a transimpedance amplifier [14] and the deflection angle measurements with the MEMS Testbench [44]. Using the frequency response of the actuated decay, the inertia of the mirror is obtained as a scaling factor. Finally, the averaged damping function is estimated from the measured response curve and corrected phase by a square rooted sine input with a 120 V peak input voltage [26].

Fig. 2 shows the normalized nonlinear stiffness function and the averaged damping function identified for the MEMS mirror [26]. The actuation torque is given by the angular derivative of the comb drive capacitor,  $dC/d\theta$ , and the time-dependent actuation voltage,  $V(t)$ . The resonant MEMS mirror is parametrically excited by the voltage input, i.e. the trivial solution  $\theta = 0$  is unstable in certain regions of the parameter space of input amplitude and frequency, leading to resonant oscillations. The first parametric resonance is excited when the input frequency is approximately twice the mirror's natural frequency. This paper is constrained to the case of the first order resonance since it is much more efficient compared to higher order resonances and thus of dominant interest for practical purposes.

#### B. Fourier Approximation for Angular Derivative of the Comb Drive Capacitance

A Fourier series based approximation is proposed for an accurate model of the angular derivative of the comb drive capacitance as in [26]

$$\begin{aligned} \frac{dC}{d\theta} \approx & a_0(0) + \sum_{n=1}^N 2a_0(n) \cos\left(\frac{\pi n \rho_0 \theta}{N_0}\right) \\ & + \sum_{n=1}^N 2b_0(n) \sin\left(\frac{\pi n \rho_0 \theta}{N_0}\right), \end{aligned} \quad (4)$$

where  $a_0(n)$  and  $b_0(n)$  denote Fourier coefficients as

$$a_0(n) = \frac{1}{N_0} \sum_{l=-N_0/2}^{N_0/2-1} \left. \frac{dC}{d\theta} \right|_{\theta=2\rho_0^{-1}l} \cos\left(\frac{2\pi nl}{N_0}\right), \quad (5)$$

$$b_0(n) = \frac{1}{N_0} \sum_{l=-N_0/2}^{N_0/2-1} \left. \frac{dC}{d\theta} \right|_{\theta=2\rho_0^{-1}l} \sin\left(\frac{2\pi nl}{N_0}\right), \quad (6)$$

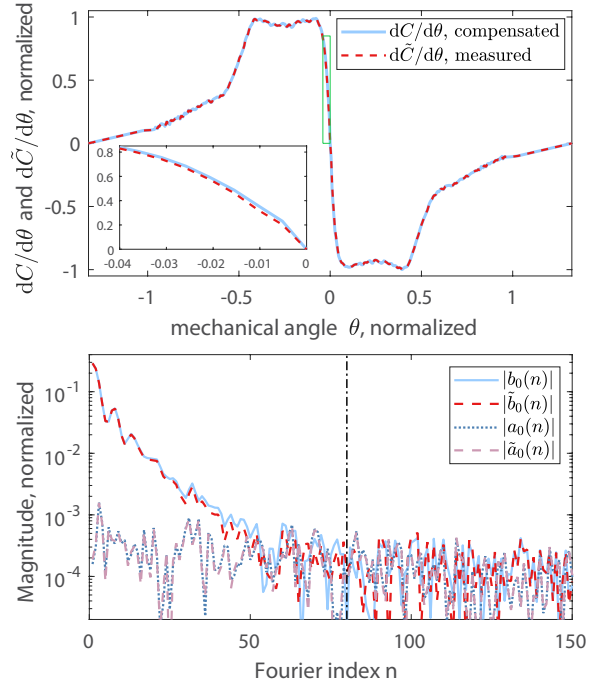


Fig. 3. (top) Measured and compensated angular derivative of the comb drive capacitance. (bottom) Magnitude of Fourier coefficients of the compensated  $dC/d\theta$ , i.e.  $a_0(n)$  and  $b_0(n)$ , compared to those of the measurements  $dC/d\theta$ , i.e.  $\tilde{a}_0(n)$  and  $\tilde{b}_0(n)$ . A black dashed-dot line indicates  $N = 80$ .

and  $N$  denotes a finite number of summands for the approximation and  $N_0$  denotes an even number for discretization of the comb drive capacitance for discrete Fourier transform (DFT). A scaling factor  $\rho_0$  defines a span to the maximum amplitude  $\Theta_{\max}$ , i.e.  $\rho_0 = N_0/\Theta_{\max}$ . The maximum amplitude is chosen to be an angle larger than the range of the scanning angle since (4) defines  $dC/d\theta$  as a function of period  $2\Theta_{\max}$  and the approximation is consequently not valid for  $|\theta| > \Theta_{\max}$ .  $\Theta_{\max}$  can be any value up to  $\pi$ . Considering computational efficiency, however, the choice close to, but slightly larger than the maximum target amplitude is preferential. For a good convergence of (4) in a finite  $N$ , an extrapolation to zero at the negative and positive maximum amplitude, i.e.  $-\Theta_{\max}$  and  $\Theta_{\max}$ , is used to eliminate the discontinuity at each end [26].

The angular derivative of the comb capacitance is obtained by current sensing of the comb drives [14], but it can be distorted by the characteristics of the employed measurement circuit, e.g. its bandwidth, and slew rate, resulting in a gradient reduction at the zero crossing [30]. To heal such distortion, a local compensation near zero angle is considered by a Gaussian-like function as

$$\frac{dC}{d\theta} = \left(1 + \alpha_1 e^{-0.5\lambda_1^{-2}\theta^2} + \alpha_2 e^{-0.5\lambda_2^{-2}\theta^4}\right) \frac{d\tilde{C}}{d\theta}, \quad (7)$$

where  $d\tilde{C}/d\theta$  denotes the measured angular derivative of the comb drive capacitance,  $\lambda_1$  and  $\lambda_2$  are derivation parameters for the local distortion near the zero crossing, and  $\alpha_1$  and

$\alpha_2$  denote scaling factors for compensation. Two sets of parameters ( $\alpha_1, \lambda_1$ ) and ( $\alpha_2, \lambda_2$ ) generate the slope changes near the zero crossing and are manually adjusted based on frequency responses at low and zero amplitudes by inputs with a square rooted sine waveform.

Fig. 3 illustrates the measured and the compensated angular derivative of the comb drive capacitance and their Fourier coefficients. The measured  $d\tilde{C}/d\theta$  function reflects the combination of an inner comb drive and an outer comb drive at each side of the rotation axis in Fig. 1. As a consequence of their placement, the former exerts a weak torque, but in a wide angle range, while the latter creates a stronger torque, but in a narrower angle range. This results in a high but narrow plateau with negative and positive torque at small positive and negative angles, respectively, up to approximately  $\pm 0.45$  and two distinct sections with approximately linear slopes at larger amplitudes over  $\pm 0.48$ . The overall torque function has odd symmetry due to the symmetric design of the comb drives and the use of the same layer for stator and rotor electrodes. Around zero, the torque sharply transits from the positive plateau to the negative plateau. To compensate the measurement error near the zero angle, the slope of the compensated derivative near zero crossing is about 14 % steeper than in the measurements, while the values at other angles are the same. This increases the high frequency Fourier components. For a more accurate approximation of the zero crossing,  $N$  should be at least 80, which increases the dimension of the calculation. As discussed in [26],  $N = 50$  is still sufficient to accurately describe stationary solutions at large amplitudes, e.g. on the top response curve, with reduced computation effort (cf. Sec. IV-A).

### C. Fourier Approximation of General Voltage Inputs

The voltage input to the comb drives can be approximated by a limited number of harmonics  $M$ , i.e.

$$|V(t)| \approx U \sqrt{u_c(t)}, \quad (8)$$

$$u_c(t) = \frac{a_u(0)}{2} + \sum_{m=1}^M a_u(m) \cos(m\Omega t) + \sum_{m=1}^M b_u(m) \sin(m\Omega t), \quad (9)$$

where  $u_c$  denotes a non-negative general input waveform, whose maximum is set to 1 without loss of generality, and  $U$  denotes a peak input voltage. The Fourier coefficients of the input waveform are defined as

$$a_u(m) = \frac{2}{T_\Omega} \int_{T_\Omega} u_c(t) \cos(m\Omega t) dt, m \in 0, 1, \dots, \quad (10)$$

$$b_u(m) = \frac{2}{T_\Omega} \int_{T_\Omega} u_c(t) \sin(m\Omega t) dt, m \in 1, 2, \dots, \quad (11)$$

where  $T_\Omega$  denotes the period of the input signal, i.e.  $T_\Omega = 2\pi/\Omega$ . With  $M_0$  samples per a period, DFT approximates the

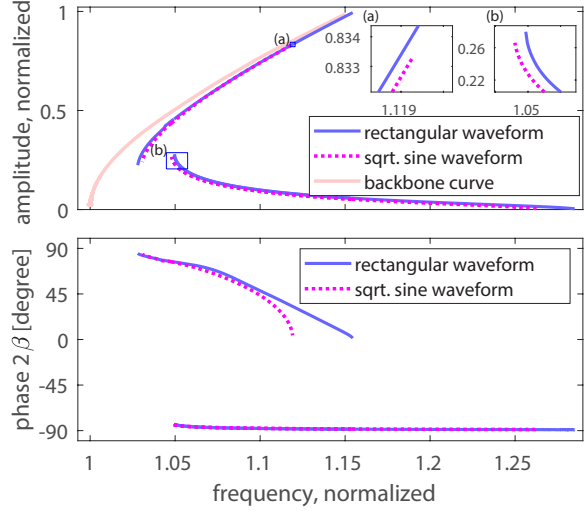


Fig. 4. Measured frequency response and frequency-phase plot from a square rooted sine input waveform and a rectangular input waveform of 0.5 duty cycle. Both have a 90 V peak input voltage and the phase of the square rooted sine input waveform is shifted for matching the synchronized excitation.

coefficients for a finite number  $M \leq M_0/2$  as

$$a_u(m) = \frac{2}{M_0} \sum_{i=1}^{M_0} u_c(t_i) \cos(m\Omega t_i), \quad (12)$$

$$b_u(m) = \frac{2}{M_0} \sum_{i=1}^{M_0} u_c(t_i) \sin(m\Omega t_i), \quad (13)$$

where  $t_i$  denotes  $i$ -th discrete time sample  $t_i \in (0, T_\Omega)$  and  $i$  is the index of the time slices.

Fig. 4 illustrates the measured frequency responses and frequency-phase plots of the MEMS mirror with a square rooted sine input waveform and a rectangular input waveform with the peak input voltage 90 V for both. The frequency responses are similar while the rectangular voltage input can reach 20 % larger amplitudes than the square rooted sine voltage input. The phases at high amplitudes show a significant difference: the frequency-phase plot from the square rooted input waveform has a parabola shape while the frequency-phase plot from the rectangular input waveform is characterized by two linear functions. This demonstrates that these frequency and phase responses cannot be accurately described by superposition, but require a dedicated analysis due to the nonlinear structure of (1).

## III. ANALYTIC MODEL OF THE MEMS MIRROR WITH A GENERAL VOLTAGE INPUT

### A. Slow Flow Model of the MEMS Mirror with a General Voltage Input

By introducing a dimensionless state variable  $x = \theta/\theta_0$ , amplitude  $A = \Theta/\theta_0$ , normalized time  $\tau = t/t_0$  where  $t_0 = \sqrt{I/k_1}$ , and normalized actuation frequency  $\Omega_a = \Omega t_0$ . A



dimensionless dynamic equation can be derived from (1), (4), and (8) as

$$\begin{aligned} & \ddot{x} + 2\mu(A)\dot{x} + x + K_3x^3 + K_5x^5 + K_7x^7 \\ & = U^2 \left( a_u(0) + \sum_{m=1}^M 2a_u(m) \cos(m\Omega_a\tau) + 2b_u(m) \sin(m\Omega_a\tau) \right) \\ & \times \left( \frac{1}{2}a(0) + \sum_{n=1}^N a(n) \cos(\rho nx) + b(n) \sin(\rho nx) \right), \end{aligned} \quad (14)$$

where the dimensionless damping and stiffness coefficients and actuation parameters are defined by

$$\begin{aligned} \mu(A) &= \frac{c(A\theta_0)t_0}{2I}, \quad K_3 = \frac{k_3\theta_0^2t_0^2}{I}, \quad K_5 = \frac{k_5\theta_0^6t_0^2}{I}, \quad K_7 = \frac{k_7\theta_0^6t_0^2}{I}, \\ a(n) &= \frac{t_0^2a_0(n)}{2I\theta_0}, \quad b(n) = \frac{t_0^2b_0(n)}{2I\theta_0}, \quad \rho = \frac{\pi\theta_0\rho_0}{N_0}. \end{aligned} \quad (15)$$

In the further derivation, only sine terms  $b(n)$  in the actuator model of (4) are considered and the constant and cosine terms  $a(n)$  are neglected, the reason for which is discussed later (cf. Cor. 2). Based on perturbation theory [45], [46], Eq. (14) can be rewritten as

$$\begin{aligned} & \ddot{x} + \sigma^2 x = \epsilon \left[ -2\mu(A)\dot{x} - K_3x^3 - K_5x^5 - K_7x^7 \right. \\ & + (\sigma^2 - 1)x + U^2a_u(0) \sum_{n=1}^N b(n) \sin(\rho nx) \\ & + 2U^2 \sum_{n=1}^N \sum_{m=1}^M b(n)a_u(m) \sin(\rho nx) \cos(m\Omega_a\tau) \\ & \left. + 2U^2 \sum_{n=1}^N \sum_{m=1}^M b(n)b_u(m) \sin(\rho nx) \sin(m\Omega_a\tau) \right], \end{aligned} \quad (16)$$

where  $\epsilon$  is a dimensionless parameter, used as a bookkeeping device [45], [47], [48]. The value of  $\epsilon$  scales the nonlinearity and  $\epsilon = 1$  means the full nonlinearity [46], [47]. The parameter  $\sigma$  denotes the normalized frequency of the mirror, given by one half of the actuation frequency, i.e.  $\sigma = \Omega_a/2$ , in the first order parametric resonance. The term of  $\sigma$  on the right hand side corrects the frequency error compared to the natural frequency on the left hand side [46]. Following perturbation theory, the solution can be decomposed as  $x = x_0 + \epsilon x_1$  and the time scales can be written as  $T_i = \epsilon^i \tau$ , i.e.  $T_0 = \tau$ ,  $T_1 = \epsilon\tau$ . The partial derivative operators are defined as  $D_i = \frac{\partial}{\partial T_i}$ , i.e.  $D_0 = \frac{\partial}{\partial T_0}$  and  $D_1 = \frac{\partial}{\partial T_1}$ . Only considering terms of order  $\epsilon^0$  and  $\epsilon^1$ , Eq. (16) is rewritten as

$$D_0^2 x_0 + \sigma^2 x_0 = 0, \quad (17)$$

$$D_0^2 x_1 + \sigma^2 x_1 = \Psi(x_0, \sigma, T_0) - 2D_0 D_1 x_0, \quad (18)$$

where a nonlinear function  $\Psi$  is defined by

$$\begin{aligned} \Psi(x_0, \sigma, T_0) &= -2\mu(A)D_0 x_0 + (\sigma^2 - 1)x_0 - K_3x_0^3 - K_5x_0^5 \\ &- K_7x_0^7 + U^2a_u(0) \sum_{n=1}^N b(n) \sin(\rho nx_0) \\ &+ 2U^2 \sum_{n=1}^N \sum_{m=1}^M b(n)a_u(m) \sin(\rho nx_0) \cos(2m\sigma T_0) \\ &+ 2U^2 \sum_{n=1}^N \sum_{m=1}^M b(n)b_u(m) \sin(\rho nx_0) \sin(2m\sigma T_0). \end{aligned}$$

The ordinary undamped harmonic oscillator in (17) yields

$$x_0 = A(T_1) \cos(\sigma T_0 + \beta(T_1)), \quad (19)$$

where  $A(T_1)$  and  $\beta(T_1)$  denote the dimensionless amplitude and phase, respectively, which evolve in slow time  $T_1$ . The dimensionless amplitude has already been used in the description of the averaged nonlinear damping function. By the solvability condition [45], [46], [48], the solution of (17) and (18) satisfies

$$\int_0^{2\pi} [\Psi(x_0, \sigma, T_0) - 2D_0 D_1 x_0] e^{-i\omega} d\omega = 0, \quad (20)$$

where  $\omega = \sigma T_0 + \beta(T_1)$ . For the calculation of these averaging integrals of the comb drive capacitance in (20), a lemma and a corollary in [26] are extended as follows.

**Lemma 1.** *The average over a period for the sine terms of the comb drive torque in (4) is given by*

$$\begin{aligned} & \int_0^{2\pi} \sin(\rho n A \cos \omega) \cos \omega \cos(2m\omega - 2m\beta) d\omega \\ &= \pi (-1)^m (J_{2m+1}(\rho n A) - J_{2m-1}(\rho n A)) \cos(2m\beta) \\ &= 2\pi (-1)^m \left( \frac{2m}{\rho n A} J_{2m}(\rho n A) - J_{2m-1}(\rho n A) \right) \cos(2m\beta), \end{aligned} \quad (21)$$

$$\begin{aligned} & \int_0^{2\pi} \sin(\rho n A \cos \omega) \sin \omega \cos(2m\omega - 2m\beta) d\omega \\ &= \pi (-1)^m (-J_{2m+1}(\rho n A) - J_{2m-1}(\rho n A)) \sin(2m\beta) \\ &= 2\pi (-1)^m \left( -\frac{2m}{\rho n A} J_{2m}(\rho n A) \right) \sin(2m\beta), \end{aligned} \quad (22)$$

$$\begin{aligned} & \int_0^{2\pi} \sin(\rho n A \cos \omega) \cos \omega \sin(2m\omega - 2m\beta) d\omega \\ &= \pi (-1)^m (-J_{2m+1}(\rho n A) + J_{2m-1}(\rho n A)) \sin(2m\beta) \\ &= 2\pi (-1)^m \left( -\frac{2m}{\rho n A} J_{2m}(\rho n A) + J_{2m-1}(\rho n A) \right) \sin(2m\beta), \end{aligned} \quad (23)$$

$$\begin{aligned} & \int_0^{2\pi} \sin(\rho n A \cos \omega) \sin \omega \sin(2m\omega - 2m\beta) d\omega \\ &= \pi (-1)^m (-J_{2m+1}(\rho n A) - J_{2m-1}(\rho n A)) \cos(2m\beta) \\ &= 2\pi (-1)^m \left( -\frac{2m}{\rho n A} J_{2m}(\rho n A) \right) \cos(2m\beta), \end{aligned} \quad (24)$$

where  $J_\nu(z)$  is the Bessel function of the first kind.

**Corollary 2.** *The average over a period for the cosine terms of the comb drive torque in (4) is given by*

$$\int_0^{2\pi} \cos(\rho n A \cos \omega) \cos \omega \cos(2m\omega - 2m\beta) d\omega = 0, \quad (25)$$

$$\int_0^{2\pi} \cos(\rho n A \cos \omega) \sin \omega \cos(2m\omega - 2m\beta) d\omega = 0, \quad (26)$$

$$\int_0^{2\pi} \cos(\rho n A \cos \omega) \cos \omega \sin(2m\omega - 2m\beta) d\omega = 0, \quad (27)$$

$$\int_0^{2\pi} \cos(\rho n A \cos \omega) \sin \omega \sin(2m\omega - 2m\beta) d\omega = 0. \quad (28)$$

The proof of the lemma and corollary is given in Appendix A. Corollary 2 means that the terms with  $a(n)$  including  $a(0)$ , which model an asymmetry and an offset of the comb drive torque, do not influence the first order parametric oscillation because their contributions are annihilated when  $\sigma = \Omega_a/2$ , as discussed in [26]. Corollary 2 generalizes

from [26] that this explanation holds regardless of the input waveform.

By Lemma 1 and Corollary 2, the slow flow amplitude and phase dynamics of the solution (19) with a generalized input can be obtained for positive amplitude, i.e.  $A > 0$ , as

$$\begin{aligned} \frac{dA}{dT_1} &= -A\mu(A) - \frac{U^2}{\sigma} \mathbf{b}_N \mathbf{J}_A (\mathbf{D}_{a_M} \mathbf{b}_s + \mathbf{D}_{b_M} \mathbf{b}_c) \quad (29) \\ \frac{d\beta}{dT_1} &= \frac{3K_3 A^2}{8\sigma} + \frac{5K_5 A^4}{16\sigma} + \frac{35K_7 A^6}{128\sigma} - \frac{(\sigma^2 - 1)}{2\sigma} \\ &\quad - \frac{U^2}{\sigma A} \mathbf{b}_N (a_u(0) \mathbf{J}_0 + \mathbf{J}_\beta (\mathbf{D}_{a_M} \mathbf{b}_c - \mathbf{D}_{b_M} \mathbf{b}_s)), \quad (30) \end{aligned}$$

where dynamic influence matrices for amplitude and phase  $\mathbf{J}_A, \mathbf{J}_\beta \in \mathbb{R}^{N \times M}$  and a zero frequency dynamic influence vector  $\mathbf{J}_0 \in \mathbb{R}^N$  are used, whose elements are defined by

$$\mathbf{J}_{A(n,m)} = (-1)^{m+1} (J_{2m-1}(\rho n A) + J_{2m+1}(\rho n A)), \quad (31)$$

$$\mathbf{J}_{\beta(n,m)} = (-1)^{m+1} (J_{2m-1}(\rho n A) - J_{2m+1}(\rho n A)), \quad (32)$$

$$\mathbf{J}_{0(n,1)} = J_1(\rho n A), \quad (33)$$

and the torque component vector  $\mathbf{b}_N \in \mathbb{R}^N$  and the input frequency component vector  $\mathbf{a}_M$  and  $\mathbf{b}_M \in \mathbb{R}^M$  are respectively defined by

$$\mathbf{b}_N = [b(1) \ b(2) \ \cdots \ b(N)]^T, \quad (34)$$

$$\mathbf{a}_M = [a_u(1) \ a_u(2) \ \cdots \ a_u(M)]^T, \quad (35)$$

$$\mathbf{b}_M = [b_u(1) \ b_u(2) \ \cdots \ b_u(M)]^T, \quad (36)$$

where  $\mathbf{v}^T$  denotes the transpose operator of the vector  $\mathbf{v}$  and  $\mathbf{D}_v$  denotes the diagonalized matrix of a vector  $\mathbf{v}$ . The cosine and sine term of integer scaled double phase  $\mathbf{b}_c, \mathbf{b}_s \in \mathbb{R}^M$  are defined by

$$\mathbf{b}_c = [\cos 2\beta \ \cos 4\beta \ \cdots \ \cos(2M\beta)]^T, \quad (37)$$

$$\mathbf{b}_s = [\sin 2\beta \ \sin 4\beta \ \cdots \ \sin(2M\beta)]^T. \quad (38)$$

The detailed derivation is given in Appendix B. For general inputs of (8), the slow flow model of (29) and (30) approximates the global dynamics for given input frequency  $\sigma$ , amplitude  $A$ , and phase  $\beta$  while it does not provide a closed form solution of primary frequencies as in the case of a square rooted sine input [26]. Instead, the stationary solutions can be obtained numerically (cf. Sec. III-D).

In addition to the global evolution equations, the local dynamics for an operating point can be written as [49]

$$\begin{aligned} A_i(T_1) &= \bar{A}_i + \varepsilon \xi(T_1), \\ \beta_i(T_1) &= \bar{\beta}_i + \varepsilon \zeta(T_1), \end{aligned} \quad (39)$$

where  $\xi$  and  $\zeta$  denote local deviations of the amplitude and phase, respectively.  $\bar{A}_i$  and  $\bar{\beta}_i$  are the stationary amplitude and the phase of the  $i$ -th equilibrium at the specific frequency  $\sigma$ , respectively, defining the operating point. A dimensionless parameter  $\varepsilon$  is introduced for local dynamics derivation. This leads to a Jacobian matrix at the operating point defined by

$$\begin{bmatrix} \dot{\xi} \\ \dot{\zeta} \end{bmatrix} = \begin{bmatrix} A_{11} & A_{12} \\ A_{21} & A_{22} \end{bmatrix} \begin{bmatrix} \xi \\ \zeta \end{bmatrix}, \quad (40)$$

where the elements are

$$A_{11} = - \left( \frac{d(\bar{A}_i \mu(\bar{A}_i))}{d\bar{A}_i} + \frac{U^2}{\sigma} \mathbf{b}_N \bar{\mathbf{J}}_{dA} (\mathbf{D}_{a_M} \bar{\mathbf{b}}_s + \mathbf{D}_{b_M} \bar{\mathbf{b}}_c) \right), \quad (41)$$

$$A_{12} = - \frac{U^2}{\sigma} \mathbf{b}_N \bar{\mathbf{J}}_A (\mathbf{D}_{a_M} \mathbf{D}_{2M} \bar{\mathbf{b}}_c - \mathbf{D}_{b_M} \mathbf{D}_{2M} \bar{\mathbf{b}}_s), \quad (42)$$

$$\begin{aligned} A_{21} &= \frac{3K_3 \bar{A}_i}{4\sigma} + \frac{5K_5 \bar{A}_i^3}{4\sigma} + \frac{105K_7 \bar{A}_i^5}{64\sigma} \\ &\quad + \frac{U^2}{\sigma} \mathbf{b}_N (a_u(0) \bar{\mathbf{J}}_{d0} - \bar{\mathbf{J}}_{d\beta} (\mathbf{D}_{a_M} \bar{\mathbf{b}}_c - \mathbf{D}_{b_M} \bar{\mathbf{b}}_s)), \quad (43) \end{aligned}$$

$$A_{22} = \frac{U^2}{\sigma \bar{A}_i} \mathbf{b}_N \bar{\mathbf{J}}_\beta (\mathbf{D}_{a_M} \mathbf{D}_{2M} \bar{\mathbf{b}}_s + \mathbf{D}_{b_M} \mathbf{D}_{2M} \bar{\mathbf{b}}_c), \quad (44)$$

where  $\bar{\mathbf{J}}_A$  and  $\bar{\mathbf{J}}_\beta$  are dynamic influence matrices for amplitude (31) and phase (32) of  $i$ -th equilibrium, respectively, and  $\bar{\mathbf{b}}_c$  and  $\bar{\mathbf{b}}_s$  are also the cosine and sine terms of integer scaled double phase in (37) and (38) with  $\bar{\beta}_i$ .  $\bar{\mathbf{J}}_{dA}$ ,  $\bar{\mathbf{J}}_{d\beta}$ , and  $\bar{\mathbf{J}}_{d0}$  denote the amplitude derivatives of the dynamic influence matrices and vector, whose elements are given by

$$\bar{\mathbf{J}}_{dA(n,m)} = (-1)^{m+1} \frac{\rho n}{2} (J_{2m-2}(\rho n \bar{A}_i) - J_{2m+2}(\rho n \bar{A}_i)), \quad (45)$$

$$\begin{aligned} \bar{\mathbf{J}}_{d\beta(n,m)} &= \frac{(-1)^{m+1}}{\bar{A}_i^2} \left( - (J_{2m-1}(\rho n \bar{A}_i) - J_{2m+1}(\rho n \bar{A}_i)) + \frac{\rho n \bar{A}_i}{2} \right. \\ &\quad \times (J_{2m-2}(\rho n \bar{A}_i) - 2J_{2m}(\rho n \bar{A}_i) + J_{2m+2}(\rho n \bar{A}_i)) \Big), \quad (46) \end{aligned}$$

$$\bar{\mathbf{J}}_{d0(n,1)} = \frac{1}{\bar{A}_i} \rho n J_2(\rho n \bar{A}_i), \quad (47)$$

and a scaling matrix is defined by

$$\mathbf{D}_{2M} = \text{diag}([2 \ 4 \ \cdots \ 2M]). \quad (48)$$

The amplitude derivatives of the dynamic influence matrices are obtained by the derivative of the Bessel function using the following Bessel identities

$$\frac{d}{d\bar{A}_i} J_\nu(\rho n \bar{A}_i) = \frac{\rho n}{2} (J_{\nu-1}(\rho n \bar{A}_i) - J_{\nu+1}(\rho n \bar{A}_i)),$$

$$\frac{d}{d\bar{A}_i} \bar{A}_i^{-\nu} J_\nu(\rho n \bar{A}_i) = -\rho n \bar{A}_i^{-\nu} J_{\nu+1}(\rho n \bar{A}_i).$$

The Jacobian matrix plays an important role for determining the stability of a equilibrium solution and the local dynamics near the steady state solution. The local dynamics are used for design of the control and analysis of the vibration influence [22], [35].

### B. Dynamic Influence Matrices and Vectors

The dynamic influence matrices  $\mathbf{J}_A, \mathbf{J}_\beta, \bar{\mathbf{J}}_{dA}, \bar{\mathbf{J}}_{d\beta}$ , and dynamic influence vectors  $\mathbf{J}_0$  and  $\bar{\mathbf{J}}_{d0}$  are uniquely defined by the amplitude of the oscillator and are not dependent on the shape of the comb drives and the input waveform. The choice of the scaling factor  $\rho_0$  does not affect the dynamic influence matrices and vectors, either. The elements of the matrices describe a weighted mapping of the frequency components of the angular derivative of the comb drive capacitance and the input waveform to the slow flow mirror dynamics.

Fig. 5 illustrates normalized absolute values of the matrix elements from the dynamic influence matrices  $\mathbf{J}_A$  and  $\mathbf{J}_\beta$  for amplitudes of 0.1, 0.5, and 1.0 and from the dynamic influence matrices, weighted by the comb drive torque, i.e.  $\mathbf{D}_{b_N} \mathbf{J}_A$

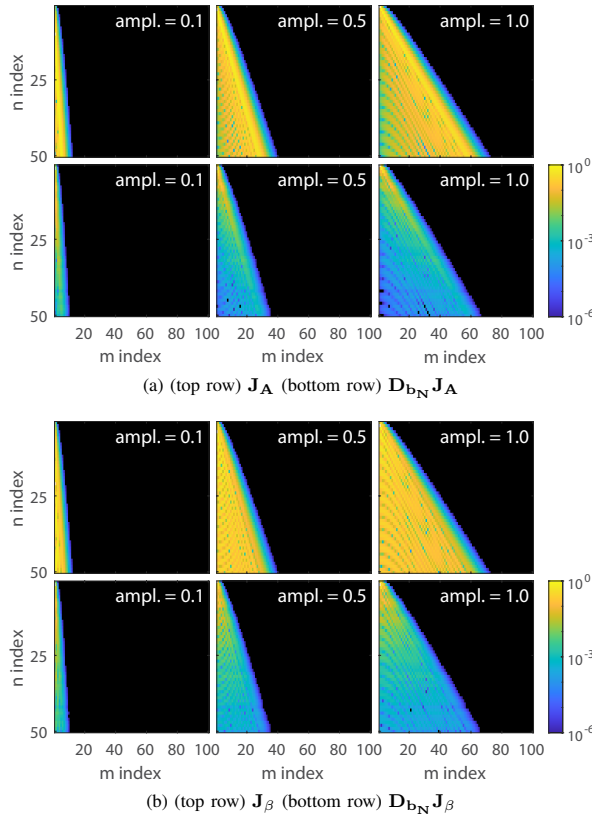


Fig. 5. The normalized absolute element values of dynamic influence matrices  $\mathbf{J}_A$  and  $\mathbf{J}_\beta$  and the weighted dynamic influence matrices scaled by the comb drive torque,  $\mathbf{D}_{b_N}\mathbf{J}_A$  and  $\mathbf{D}_{b_N}\mathbf{J}_\beta$ , plotted according to the comb drive frequency component index  $n$  and the input frequency component index  $m$ . The absolute values of the elements of the matrix are normalized by the maximum element of the matrix. The maximum element is drawn in white and elements less than  $10^{-6}$  of the maximum element are depicted in black.

and  $\mathbf{D}_{b_N}\mathbf{J}_\beta$ . (See the supplementary movie S1 for evolution of dynamic influence matrices with amplitude.) The absolute values of the elements in the matrices are normalized by the maximum value of the elements to illustrate the structure of the matrices. It reveals that the effective frequency components  $m$  of the input waveform to the mirror dynamics are determined by both the amplitude  $A$  of the oscillator and frequency components  $n$  of the comb drive torque. Low frequency components of the input waveform influence the dynamics at low amplitudes, and the high frequency components of the input waveform increase their influences as the amplitude becomes larger. In addition, high frequency components of the input only couple to the high frequency components of the comb drive torque. This is reflected by large zero regions in the right upper side of the dynamic influence matrices, which is due to properties of Bessel function [50]. This influence is weighted by the torque function via  $\mathbf{D}_{b_N}$ , which reduces the influence of high- $n$  matrix entries and results in a dominance of low frequency components.

Since the comb drive torque is typically band-limited, the effective bandwidth of the input waveform is also limited by

the target maximum amplitude of the oscillator. For this reason, the ripples of Gibbs phenomenon in the input waveform [19] do not influence the first order slow flow mirror dynamics as long as a sufficient number of harmonics,  $M$ , is considered in the input. In the case of Fig. 5,  $M = 78$  for  $N = 50$ , e.g. 312 kHz for 2 kHz mirror frequency, is sufficient to cover the amplitude of 1. This can be used to determine the bandwidth of the driving circuitry without harming the maximum amplitude. Since this analysis implies an approximation (19), it only holds for a weakly nonlinear oscillator, as implicitly defined by its expansion in a power series in  $\epsilon$  (16).

### C. Asymptotic Behavior at Zero Amplitude

This section investigates the instability of (1) based on the derived slow flow model. The behavior at zero amplitude can be analyzed asymptotically using a slow flow model, considering an oscillation with an infinitely small amplitude. Using  $\lim_{A \rightarrow 0} J_\nu(\rho mA)/A^\nu = (\rho n)^\nu/(2^\nu \nu!)$  by L'Hôpital's rule, the asymptotic values of the dynamic influence matrices and vectors at zero amplitudes are given as

$$\lim_{A \rightarrow 0} \mathbf{J}_{A(n,m)} = 0, \quad \forall n, m, \quad (49)$$

$$\lim_{A \rightarrow 0} A^{-1} \mathbf{J}_\beta(n,m) = \begin{cases} \frac{\rho n}{2}, & m = 1 \text{ and } \forall n, \\ 0, & m \neq 1 \text{ and } \forall n, \end{cases} \quad (50)$$

$$\lim_{A \rightarrow 0} A^{-1} \mathbf{J}_0 = \frac{\rho}{2} \begin{bmatrix} 1 & 2 & \cdots & N \end{bmatrix}^T = \mathbf{J}_Z, \quad (51)$$

where  $\mathbf{J}_Z$  is the zero amplitude dynamic influence vector. This leads to the asymptotic slow flow dynamics at zero amplitudes as

$$\lim_{A \rightarrow 0} \frac{dA}{dT_1} = 0, \quad (52)$$

$$\lim_{A \rightarrow 0} \frac{d\beta}{dT_1} = -\frac{(\sigma^2 - 1)}{2\sigma} - \frac{1}{\sigma} U^2 \mathbf{b}_N \mathbf{J}_Z \times (a_u(0) + a_u(1) \cos 2\beta - b_u(1) \sin 2\beta). \quad (53)$$

Due to the structure of the comb drive, which exerts at any position only pulling forces towards the rest position but no forces pushing the oscillator away from zero,  $\mathbf{b}_N \mathbf{J}_Z$  is a negative scalar, i.e.  $\mathbf{b}_N \mathbf{J}_Z < 0$ . Stationary solutions are given by  $d\beta/dT_1 = 0$  for  $\sigma > 0$  as

$$\sigma^2 - 1 = -2U^2 \mathbf{b}_N \mathbf{J}_Z \left( a_u(0) + \sqrt{a_u(1)^2 + b_u(1)^2} \sin \left( \arctan \left( \frac{a_u(1)}{b_u(1)} \right) - 2\beta \right) \right). \quad (54)$$

Using the inverse of the sine leads to stationary phases at zero amplitude as

$$2\beta = -\arcsin \alpha + \varphi, \quad (55)$$

$$\alpha = \left( -\frac{\sigma^2 - 1}{2U^2 \mathbf{b}_N \mathbf{J}_Z} + a_u(0) \right) / \sqrt{a_u(1)^2 + b_u(1)^2}, \quad \varphi = \arctan \frac{a_u(1)}{b_u(1)}, \quad (56)$$

where  $\alpha$  and  $\varphi$  are parameters for simplification. The phase is real valued if and only if  $|\alpha| \leq 1$ . This leads to the frequency boundaries of equilibria at zero amplitude  $\sigma_{z\pm}$  as

$$\sigma_{z\pm} = \left( 1 - 2U^2 \mathbf{b}_N \mathbf{J}_Z \left( a_u(0) \pm \sqrt{a_u(1)^2 + b_u(1)^2} \right) \right)^{\frac{1}{2}}. \quad (57)$$

The stationary phases are defined for the zero amplitude stationary frequencies of  $\sigma \in (\sigma_{z-}, \sigma_{z+})$ . From (55) with the condition of a real phase, it also follows that the stationary phase at zero amplitude is bounded as

$$-\frac{\pi}{2} + \varphi < 2\beta < \frac{\pi}{2} + \varphi. \quad (58)$$

It is observed that the total stationary phase at zero amplitude spans over a range of  $\pi$  for  $2\beta$ , and the ratio of the coefficients of the sine and cosine component in the fundamental frequency of the input signal determines the center of the stationary phase at zero amplitude. Trivially, the sine and cosine component ratio defines the phase setting of the input, and the phase definition shifts as the composition changes while equation (58) specifies that the fundamental frequency components solely determine this shift regardless of phases of high frequency input components.

The stability of the equilibrium at zero amplitude is determined by the Jacobian. The amplitude derivatives of the dynamic influence matrices and vector at zero amplitude asymptotically follow

$$\lim_{A \rightarrow 0} \bar{\mathbf{J}}_{\mathbf{d}\mathbf{A}(n,m)} = \begin{cases} \frac{\rho_n}{2}, & m = 1 \text{ and } \forall n, \\ 0, & m \neq 1 \text{ and } \forall n, \end{cases} \quad (59)$$

$$\lim_{A \rightarrow 0} \bar{\mathbf{J}}_{\mathbf{d}\beta(n,m)} = 0, \quad \forall n, m, \quad (60)$$

$$\lim_{A \rightarrow 0} \bar{\mathbf{J}}_{\mathbf{d}\mathbf{0}} = \begin{bmatrix} 0 & 0 & \cdots & 0 \end{bmatrix}^T. \quad (61)$$

With (55), this leads to a Jacobian matrix as a diagonal matrix,

$$\lim_{A_i \rightarrow 0} \begin{bmatrix} A_{11} & A_{12} \\ A_{21} & A_{22} \end{bmatrix} = \begin{bmatrix} A_{11,0} & 0 \\ 0 & A_{22,0} \end{bmatrix}, \quad (62)$$

where the diagonal components are defined by

$$A_{11,0} = -\mu_0 - \frac{1}{\sigma} U^2 \mathbf{b}_N \mathbf{J}_Z \sqrt{a_u^2(1) + b_u^2(1)} \sqrt{1 - \alpha^2}, \quad (63)$$

$$A_{22,0} = \frac{2}{\sigma} U^2 \mathbf{b}_N \mathbf{J}_Z \sqrt{a_u^2(1) + b_u^2(1)} \sqrt{1 - \alpha^2}. \quad (64)$$

Since the Jacobian matrix is diagonal, the poles are the values of diagonal components. Since  $A_{22,0} < 0$  by  $\mathbf{b}_N \mathbf{J}_Z < 0$ , the stationary solution is unstable if  $A_{11,0} > 0$ , forming a saddle point [39]. This results in the following second order inequality in  $\sigma^2$

$$\sigma^4 - 2(1 - 2\mu_0^2 - 2U^2 \mathbf{b}_N \mathbf{J}_Z a_u(0)) \sigma^2 + 1 - 4(U^2 \mathbf{b}_N \mathbf{J}_Z)^2 \times (a_u^2(1) + b_u^2(1) - a_u^2(0)) - 4U^2 \mathbf{b}_N \mathbf{J}_Z a_u(0) < 0.$$

The frequency boundaries, i.e. transition curves, are obtained by the solutions as

$$\sigma_{z\mu\pm} = \left( 1 - 2\mu_0^2 - 2U^2 \mathbf{b}_N \mathbf{J}_Z \left( a_u(0) \pm \sqrt{a_u^2(1) + b_u^2(1) + \frac{\mu_0^4 + (2U^2 \mathbf{b}_N \mathbf{J}_Z a_u(0) - 1)\mu_0^2}{(U^2 \mathbf{b}_N \mathbf{J}_Z)^2}} \right) \right)^{\frac{1}{2}}. \quad (65)$$

This shows that only the constant and fundamental frequency components of the input waveform influence the phase, stationary and unstable regions at zero amplitude. This trend is also observed in the dynamic influence matrices at low amplitudes in Fig 5. The resulting criterion has a simple closed

form, but it assumes the first order perturbation approximation of (19). This is verified by taking Taylor series of the approximated angular derivative of the comb drive capacitance for a small angle, i.e.  $x \ll 1$ , as

$$\sum_{n=1}^N b(n) \sin(\rho_n x) \approx 2\mathbf{b}_N \mathbf{J}_Z x, \quad (66)$$

which also approximates the electrostatic actuated stiffness term by the normalized curvature of the comb drive capacitance as

$$U^2 \frac{t_0^2}{I} \frac{d^2 C}{d\theta^2} \bigg|_{\theta=0} \approx 4U^2 \mathbf{b}_N \mathbf{J}_Z. \quad (67)$$

By (66) and with only the zero and fundamental frequency components of the input waveform, (14) results in the well known Mathieu's equation as [40]

$$\ddot{x} + 2\bar{\mu}_0 \dot{x} + (\delta + \eta \cos(\tau + \bar{\varphi}))x = 0, \quad (68)$$

where the normalized parameters are

$$\bar{\mu}_0 = \frac{\mu_0}{\Omega_a}, \quad \delta = \frac{1 - \gamma a_u(0)}{\Omega_a^2}, \quad \eta = -\frac{2\gamma \sqrt{a_u^2(1) + b_u^2(1)}}{\Omega_a^2}, \quad (69)$$

$$\bar{\varphi} = -\arctan \frac{b_u(1)}{a_u(1)}, \quad \gamma = 2U^2 \mathbf{b}_N \mathbf{J}_Z.$$

The boundaries of the instability region of (57) and (65) can be obtained by the first order approximation of the transition curves [40]. Equation (65) corresponds to the well known approximation of the transition curve in the presence of damping

$$\delta = \frac{1}{4} \pm \frac{1}{2} \sqrt{\eta^2 - 4\bar{\mu}_0^2}. \quad (70)$$

This implies that the stability analysis of the slow flow model is equivalent to the first term in Floquet theory, which is natural considering the use of the same approximation of the solution (19). Therefore (57) and (65) inherit the same limitation in accuracy by adopting a first order approximation [37], [40]. High frequency components can influence the minimum peak input voltage for instability [38] as well as the transition curves at high input voltages [40]. For small input voltages, which still includes over 100 V in the case of the used MEMS mirror and for inputs dominated by the fundamental frequency, e.g. the square rooted sine waveform or the rectangular waveform with various duty cycles, the proposed asymptotic analysis can still provide a good approximation of the stability region.

#### D. Numerical Implementation

The stationary solutions of (29) and (30) with a general input do not have a closed form, but they can be found numerically. For this calculation, a continuation technique is used for the slow flow dynamics. The initial condition is chosen by the solution considering only the constant input and the fundamental frequency, i.e.  $a_u(0)$ ,  $a_u(1)$ , and  $b_u(1)$ , which allows a closed form solution as in [26]. Then the solution with full frequency components is numerically obtained by this initial condition and stationary conditions in (29) and (30). Once a solution is found, the nearest solutions are found for



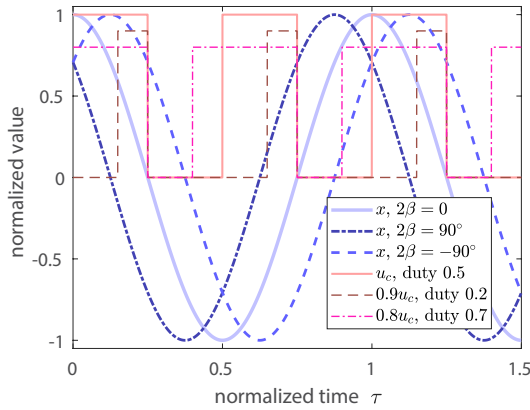


Fig. 6. Definition of the phase of the mirror and the duty cycle of the input waveform. The peak values of the input waveform are scaled for better visibility.

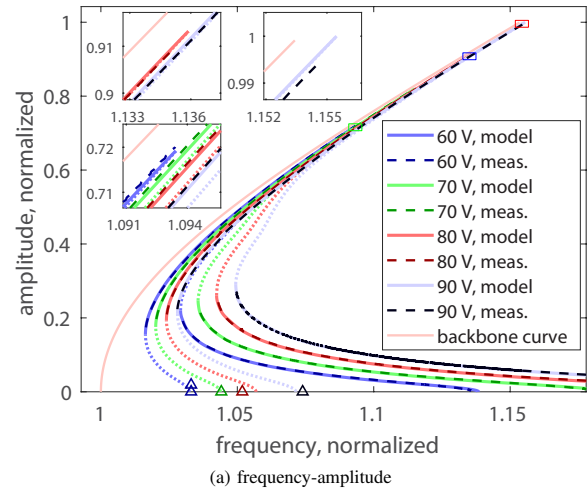
an amplitude increased or decreased by one increment using the solution as an initial value. This procedure continues until no solution is available. A nonlinear solver *fsolve* in Matlab is used for solution calculation.

This numerical calculation can be efficiently designed by calculating the dynamic influence matrices and vectors in advance since they are constant for a given amplitude and do not depend on the actuator parameters or input parameters. In addition, with a specific actuation design, expressed by  $b(n)$ , the dimension is further reduced to an inner product of vectors, removing the need of any matrix vector calculation. Although this precalculation scheme cannot be applied to describe the global dynamics, e.g. phase portraits, it can reduce the calculation time and effort for the search of the stationary solutions and for the Jacobian matrices significantly. The computation effort as well as the measurement verification of the model are evaluated in the following section.

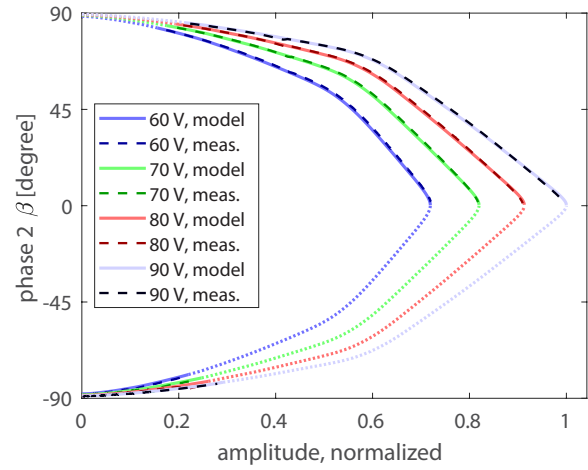
#### IV. VERIFICATION OF THE MODEL

This section describes a verification of the proposed Fourier series based slow flow model with measurement data using frequency response, transition curve, and local dynamics measurements. A MEMS test bench is used for a wide bandwidth and highly accurate MEMS deflection angle measurement, enabled by a dedicated calibration procedure [44]. The details of the employed MEMS test bench can be found in [26] and [44].

As general drive inputs to the MEMS mirror, rectangular waveforms with various duty cycles from 0.2 to 0.7 are considered since these waveforms are conveniently generated with simple high voltage generation circuitry [35]. Fig. 6 illustrates the definition of the rectangular input waveform of  $u_c$  with various duty cycles and the definition of the mirror phase with respect to the input, used in this article. To vary the duty cycle, the convention fixes the falling edge of the rectangular input at half of its period while the time of the rising edge is shifted. The convention defines zero phase to coincide with the synchronized excitation [31], [51] for a rectangular



(a) frequency-amplitude



(b) amplitude-phase

Fig. 7. Frequency response and amplitude-phase plot from the slow flow model (light solid and dotted lines) and measurements (dark dashed lines) for various peak input voltages. The stable and unstable solutions of the model are represented by solid lines and dotted lines, respectively. Dark colored triangles represent the measured lower bound of the respective unstable regions, while a double triangle represents a direct jump to the top response curve. The backbone curve is drawn with a bright pink line.

input with 0.5 duty cycle. In addition, it is also a convenient convention for the current sensing method which measures the time difference between the falling input edge and the zero crossing of the mirror current [30]. The amplitude and frequency values are normalized to the maximum amplitude reached with a 90 V input peak voltage with 0.5 duty cycle and the linear mirror frequency, respectively.

##### A. Frequency Response by Peak Input Voltages

To evaluate the accuracy of the model, the frequency response and the amplitude-phase plot are analyzed, which show a set of the stationary points of the mirror dynamics. The stable equilibria are retrieved by measuring steady-state oscillations of the MEMS mirror for given input frequencies

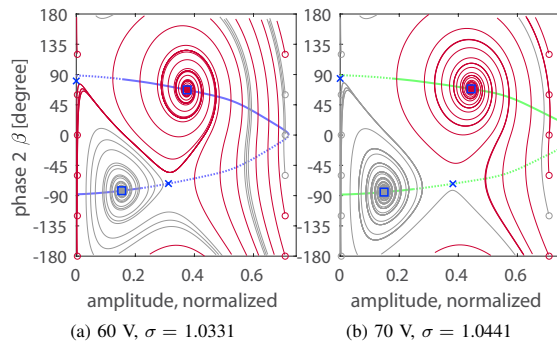


Fig. 8. Phase portraits and amplitude-phase plots (thick light colored lines) at the measured frequency of the lower bound of the zero amplitude instability region, specifically (left) frequency 1.0331 with 60 V peak input voltage and (right) frequency 1.0441 with 70 V peak input voltage. From initial conditions (circles) the slow flow dynamics lead to the stable equilibria (blue squares) while the unstable equilibria are given by blue x marks. The color of the trajectory represents its final steady state value, i.e. if it arrives at the solution of the top response curve (red) or of the bottom response curve (light gray).

where the actuation frequency is increased and decreased in increments of 2 Hz. For convenience, the stable solutions at the low amplitude side and the high amplitude side are called bottom response curve and top response curve, respectively. Due to a significantly hardening spring characteristic [26], the used mirror can usually reach the maximum amplitude on the top response curve. The lower bound of the Mathieu instability region [40] can be identified by the first unstable point in an up sweep from the stable region, where no oscillation occurs, hereafter referred to as start-up frequency.

Fig. 7a shows the frequency response of the slow flow model together with the measurement data for the rectangular input waveform with a 0.5 duty cycle. For verification, peak input voltages of 60, 70, 80, and 90 V are chosen. For all cases, the analytic solution by the slow flow model shows a good match with the measurement data at large amplitudes including the points of the bifurcation. This is mainly facilitated by the Fourier series' property as a modal approximation, which provides a good accuracy of the overall features. For large amplitudes above 0.2, normalized frequency errors are less than  $\pm 0.06\%$ , and even for small amplitudes below 0.2, the normalized frequency errors are less than  $\pm 0.47\%$ , corresponding to less than  $\pm 1.2$  Hz and  $\pm 9.4$  Hz errors for a 2 kHz linear mirror frequency, respectively. The accuracy at small amplitudes shows much improvement compared to [26] but there is still some mismatch that is not corrected by the simple correction in (7). The peak amplitude also shows a good agreement, the worst case error is 0.58 % in the 90 V peak input voltage case, which corresponds to  $0.087^\circ$  for a  $15^\circ$  amplitude. The start-up frequencies, which are obtained by the amplitude zero of the unstable solution that extends from the top response curve of the model, also show good agreement with measurements except for the case of a 80 V peak input voltage. Fig. 7b illustrates the amplitude-phase plot from the model and measurements for various peak input voltages of the rectangular waveform. The phase

variation along the amplitude is composed of two linearly shaped regions, which are different from the parabola-like shape in the square rooted sine input case while the solution lines for both input waveforms are symmetric to zero phase [26].

Contrary to the other peak input voltages, the MEMS mirror with an input at 60 V peak input voltage can directly reach the top response curve from zero amplitude at the start-up frequency. This shows that the branch eventually reached as the stationary solution from zero amplitude, i.e. either top or bottom response curve, depends on the peak input voltage. Fig. 8 illustrates two phase portraits for 60 V and 70 V peak input voltage, respectively, at the measured start-up frequencies, describing the global dynamics by (29) and (30). The initial conditions of amplitudes and phases are defined by amplitudes of 0.004 and 0.708 and phases  $k\pi/6$ ,  $k = 0, 1, \dots, 5$ , where the initial amplitude of 0.004 approximates the mirror with zero amplitude. The phase portraits of the dynamics illustrate different behaviors, reaching different stationary solutions at the top and the bottom response curve from the same approximated zero amplitude. (See supplementary movie S2 for evolution of phase portraits by frequencies.) These phase portraits also verify that the proposed slow flow model can describe the start-up behavior from zero amplitude adequately.

The simulation also demonstrates the low computational effort required by the proposed model. For evaluation, a case of  $N = 50$  is considered as a standard case for large amplitude analysis because it reduces the computation effort while the stationary frequencies of top response curves differ less than 0.0005 % from the case of  $N = 80$ . With  $N = 50$  and  $M = 100$ , the dynamic influence matrices of  $\mathbf{J}_A$ ,  $\mathbf{J}_\beta$ ,  $\bar{\mathbf{J}}_{dA}$ , and  $\bar{\mathbf{J}}_{d\beta}$  are calculated for the given amplitude points first, then the actuation vectors from the comb drive approximation are calculated for each amplitude. Using the actuation vectors, the stationary solutions and the Jacobian matrices are obtained for each peak input voltage and waveform. For 2,000 amplitude values, the dynamic influence matrix calculation takes 35.94 s, the solution calculation takes 11.33 s, and the Jacobian calculation takes 0.80 s with a Matlab 2018b script using a laptop PC (Intel Core-i7 8850H, 2.6 GHz). The simulation of the global dynamics in Fig. 8 takes 36.82 s average for a normalized time of 5000. This is 33 times longer than the single tone case, but still much less than the brute force simulation of 1303.20 s, which directly exploits (1) [14], [26].

### B. Frequency Response for Various Duty Cycles

Fig. 9 shows the frequency responses and amplitude-phase plots from the model and measurements for various duty cycles of 0.2, 0.4, 0.5, and 0.7 and peak input voltages of 60 V, 70 V and 90 V. For all cases the model shows a good agreement with the measurements like Fig. 7. It is shown that the highest maximum amplitude is achieved by the 0.5 duty cycle, and that it drops if the duty cycle deviates from 0.5. This is obvious since the energy injection of the pulling torque from the comb drive actuation is maximized for 0.5 duty cycle. The start-up frequencies decrease as the duty cycle becomes smaller since the electrostatic stiffening by the DC component of the input

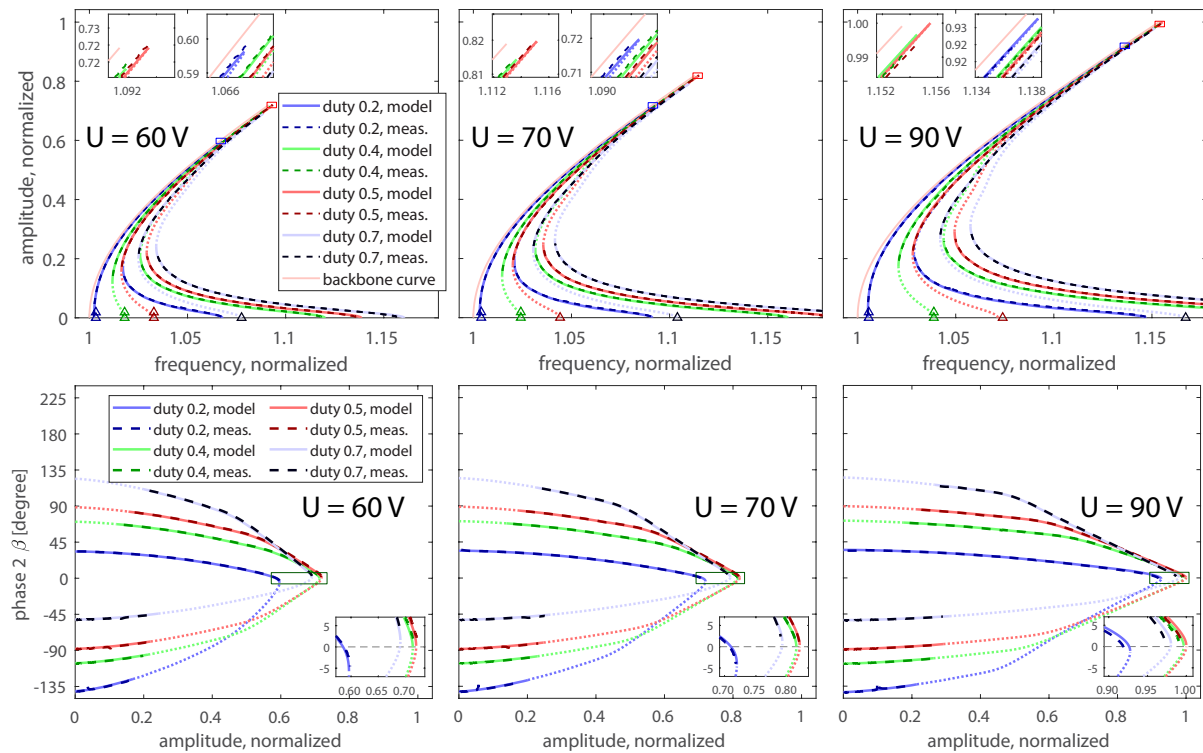


Fig. 9. Frequency responses (top figures) and amplitude-phase plots (bottom figures) from the model (light colored lines) and measurements (dark dashed lines) for various duty cycles. The representation of stability and start-up frequencies are the same as in Fig. 7.

is reduced for lower duty cycles, leading to a smaller deviation of the start-up frequency from the free oscillation frequency. In addition, a low duty cycle also allows the start-up directly to the top response curve, which is shown for all duty cycles up to 0.4. This can be used for a fast start-up strategy by omitting the transition through a bifurcation to reach the large amplitude operational point [29].

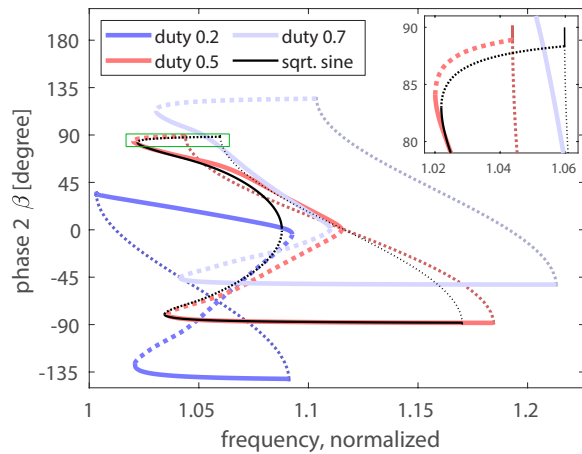
The amplitude-phase plots show more pronounced changes than the frequency response for varying duty cycle, visible in a significant asymmetry of the amplitude for positive and negative phases. The phase of the solutions deforms toward the positive phase for a large duty cycle above 0.5 and vice versa for low duty cycles below 0.5. A subtle change of the phase at the peak amplitude is found as well. This implies that zero phase is difficult to be reached for a duty cycle over 0.5 and that negative phase can be achieved by a small duty cycle below 0.5. This change of the phase at the peak amplitude is stronger when the peak input voltage decreases.

### C. Asymptotic Analysis at Zero Amplitude

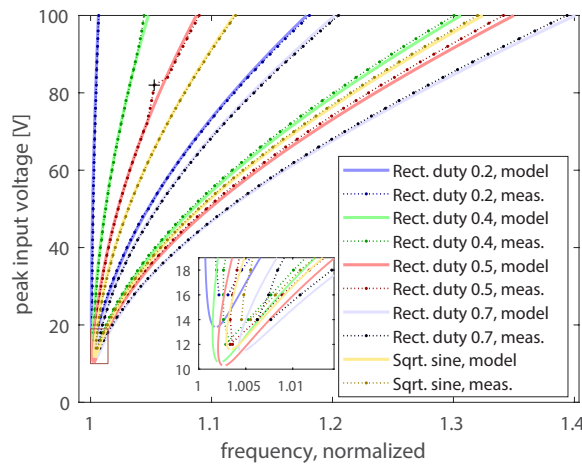
Fig. 10a illustrates a frequency-phase plot for various input waveforms with a 70 V peak input voltage including stationary points of zero amplitude. These stationary points at zero amplitude span over a range of  $\pi$  between the bounds of (58), connecting the top and the bottom response curve. The stationary points at zero amplitude shift to linear mirror

frequency as the duty cycle decreases mainly due to reduction of electrostatic stiffening at zero angle. With the amplitude-phase plots in Fig. 9, direct start-up to the top response curve with a small duty cycle can be roughly explained by the proximity of a stable equilibrium at a small amplitude on the top response curve and a saddle point at zero amplitude at the same frequency, although a global bifurcation analysis [52] or a numerical simulation as Fig. 8 are required to precisely describe it. The zoomed plot in Fig. 10a illustrates links of the non-zero amplitude response curves to the unstable equilibria at zero amplitude.

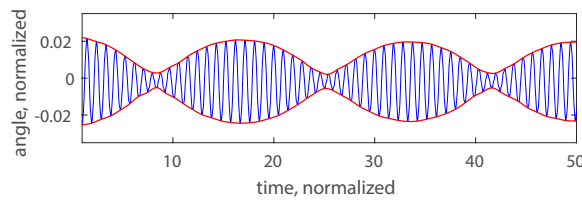
Fig. 10b depicts the renowned transition curves, delimiting the instability tongues, i.e. boundaries between parametric oscillations and no excitation [40], [53], by the model (65) and measurements for various peak input voltages and waveforms. There are mismatches around 80 V for the 0.5 duty cycle case and 90 V for the 0.4 duty cycle case, exhibiting unusual steady state quasiperiodic oscillations [40] as shown in Fig. 10c while almost all other start-up oscillations have a constant steady state amplitude. These deviations of the transition curves and exceptional quasiperiodic oscillations are possibly caused by coupling to a different rigid body mode of the mirror or high order components of the voltage input, which are largest for 0.5 duty cycle [38], but they cannot be analyzed by the first order perturbation approximation of the SDoF dynamics in (19). For low voltages, the measurements are consistent with an assumed 30 % increase in damping over the identified value,



(a) simulated frequency-phase responses



(b) simulated and measured transition curves



(c) measured steady state quasiperiodic oscillation

Fig. 10. (a) Simulated frequency-phase plot with a 70 V peak input voltage for rectangular waveforms with 0.2 to 0.7 duty cycles and a square rooted sine waveform, including equilibria at zero amplitude (finer darker lines). The stable and unstable equilibria are drawn by solid lines and dotted lines, respectively. (b) Measured and simulated transition curves of the parametric resonance for various peak input voltages and input waveforms from the model and measurements. (c) Measured steady state quasiperiodic oscillation (blue solid line) at the start-up with 0.5 duty cycle and 82 V peak input voltage (black + mark in (b)). The red solid lines show the envelope of the angular trajectory.

which can be due to the first order perturbation approximation [38] or a physical damping mechanism that is not identified by the averaging method. In general for most voltage inputs, however, the proposed model shows a good agreement with

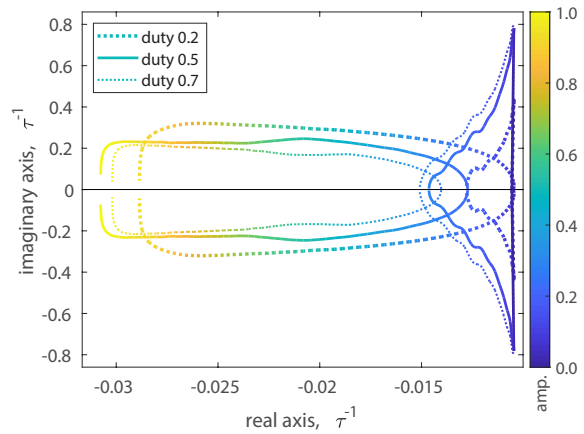


Fig. 11. Simulated evolution of the poles along the stable solutions with 90 V peak input voltage and duty cycles of 0.2, 0.5, and 0.7. The amplitude of the poles are represented by the colors of the points, illustrating the direction of the pole movement with changing amplitude.

the measurements, verifying the proposed asymptotic analysis at zero amplitude.

#### D. Local dynamics at Stable Equilibria

The local dynamics at a specific equilibrium is crucial for robustness against external disturbances [41] and the design of the control [35]. Fig. 11 describes the root locus of the complex valued poles of Jacobians of (40) for the duty cycles of 0.2, 0.5, and 0.7. The eigenfrequencies and damping ratios of the local dynamics are represented by the absolute value and the argument of the poles. Fig. 12 shows simulation and measurements of eigenfrequencies and damping ratios of the local dynamics for various duty cycles and peak input voltages. The eigenfrequencies at a given stationary amplitude of the global dynamics are increased as the peak input voltage becomes higher or the duty cycle decreases. In contrast, the damping ratio decreases as the peak input voltage becomes higher or the duty cycle decreases. Although the detailed analysis of the local dynamics is not complete by evaluation of eigenfrequency and damping ratio only, it is apparent that a trade-off between the choice of the duty cycle and the peak input voltage exists to attain the desired local dynamics. Besides, a large flat region of both eigenfrequency and damping is observed for large amplitudes, which can be regarded as beneficial operational points for a control design [35]. Overall, the simulation results show a good agreement with measurements except for a large mismatch at amplitudes near 0.4, where a mode coupling to the translational in-plane mode perpendicular to the rotation axis occurs rendering the SDoF model (1) insufficient.

These results verify that the proposed slow flow model with a Fourier based torque approximation and a Fourier-decomposed input waveform can accurately describe the behavior of a parametrically driven resonant MEMS mirror, showing potentials for the fast and accurate analysis of resonant MEMS mirror designs and their control.



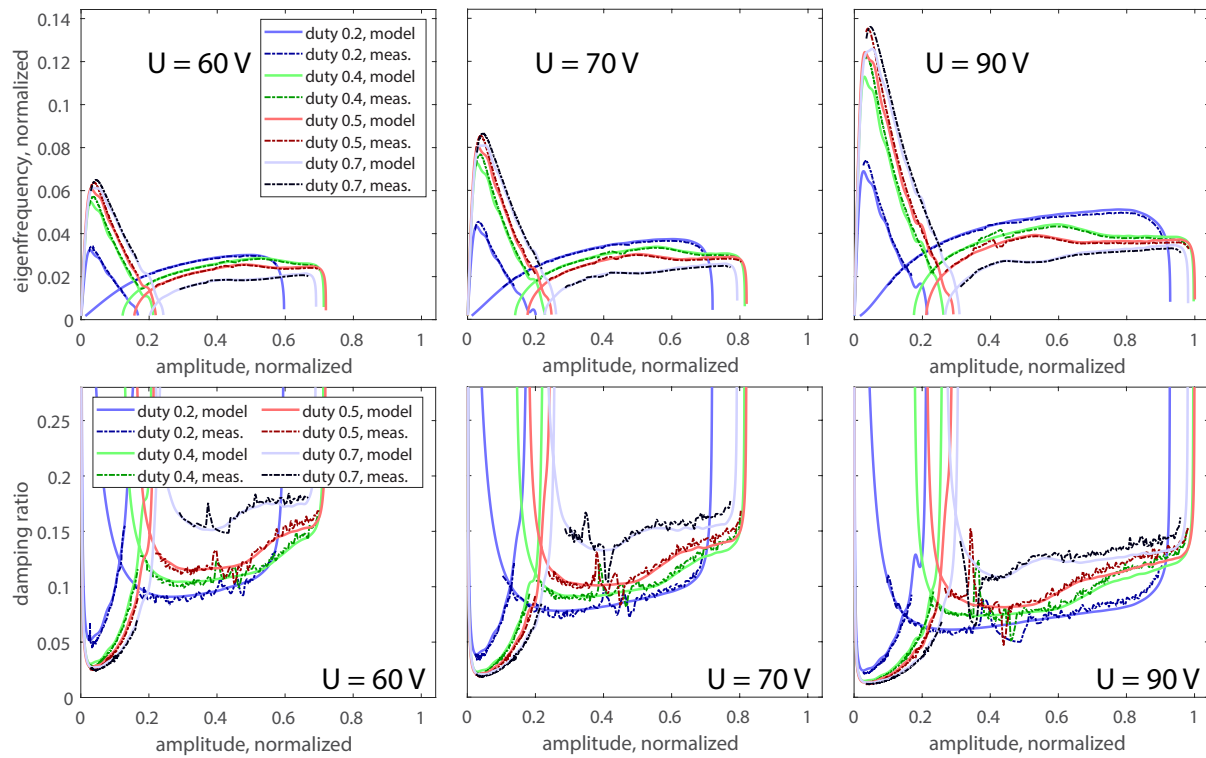


Fig. 12. Eigenfrequency and damping ratio of the simulated Jacobian matrix (light colored solid lines) and the measurements (dark colored dashed lines) for various peak input voltages and duty cycles.

## V. CONCLUSION

This paper proposes an accurate analytic model for a resonant MEMS mirror with general voltage inputs for describing its global and local dynamics. Both the nonlinear torque function and the input waveform are approximated by Fourier series with a finite number of coefficients, leading to a slow flow model and a Jacobian at equilibrium featuring dynamic influence matrices and vectors with Bessel functions. The dynamic influence matrices and vectors are only amplitude-dependent, describing the dynamic effects by frequency components of the comb drive torque and the input waveform. An analysis of the asymptotic behavior at zero amplitude reveals that only the constant and the fundamental frequency components of the input waveform influence stationary solutions and the transition curve, corresponding to a simple approximation by Mathieu's equation. The models and analysis are verified by rectangular input waveforms with various duty cycles as examples of general voltage inputs. Frequency responses demonstrate a high accuracy of the proposed model of 0.06 % and 0.47 % frequency error for large and small amplitudes, which corresponds to 1.2 Hz and 9.4 Hz peak errors for 2 kHz linear mirror frequency, respectively. Amplitude-phase plots, phase portraits, transition curves, and local dynamics demonstrate a good agreement with measurements, verifying the accuracy of the proposed model in various aspects.

The proposed analytic model can also provide practical

benefits via a wide range of accurate and efficient analyses for resonant MEMS mirrors and their control design even prior to MEMS fabrication and characterization. As demonstrated as an application example, the required bandwidth of the driving circuits can be deduced with the model from the design of the comb drive and the target amplitude. In addition, an analysis of the start-up can lead to a fast start-up strategy without transiting through a bifurcation between the bottom and the top response curve. An optimal input waveform can be also investigated considering certain target characteristics of the MEMS mirror. For robustness analysis to external vibration [41], a fast and accurate analysis of local dynamics allows an accessible design tool for a realistic performance estimation by employing the usual rectangular waveform of typical use cases. This enables a systematic design of resonant MEMS mirrors and their control for high precision and robustness applications, e.g. automotive lidars.

## APPENDIX A PROOF OF THE LEMMA

Generalized cases of Lemma 1 are given as follows.

**Lemma 3.** Consider generalized averaging integrals over a period of the motion for integers  $p$  and  $q$ . If  $p + q$  is an odd

number, the averaging integrals are given by

$$\begin{aligned} & \int_0^{2\pi} \sin(pnA \cos \omega) \cos q\omega \cos(p\omega - p\beta) d\omega \\ &= \pi \left( J_{(p-q)}(\rho nA) \sin\left(\frac{p-q}{2}\pi\right) + J_{(p+q)}(\rho nA) \sin\left(\frac{p+q}{2}\pi\right) \right) \\ & \times \cos p\beta, \end{aligned} \quad (71)$$

$$\begin{aligned} & \int_0^{2\pi} \sin(pnA \cos \omega) \sin q\omega \cos(p\omega - p\beta) d\omega \\ &= \pi \left( J_{(p-q)}(\rho nA) \sin\left(\frac{p-q}{2}\pi\right) - J_{(p+q)}(\rho nA) \sin\left(\frac{p+q}{2}\pi\right) \right) \\ & \times \sin p\beta, \end{aligned} \quad (72)$$

$$\begin{aligned} & \int_0^{2\pi} \sin(pnA \cos \omega) \cos q\omega \sin(p\omega - p\beta) d\omega \\ &= \pi \left( -J_{(p-q)}(\rho nA) \sin\left(\frac{p-q}{2}\pi\right) - J_{(p+q)}(\rho nA) \sin\left(\frac{p+q}{2}\pi\right) \right) \\ & \times \sin p\beta, \end{aligned} \quad (73)$$

$$\begin{aligned} & \int_0^{2\pi} \sin(pnA \cos \omega) \sin q\omega \sin(p\omega - p\beta) d\omega \\ &= \pi \left( J_{(p-q)}(\rho nA) \sin\left(\frac{p-q}{2}\pi\right) - J_{(p+q)}(\rho nA) \sin\left(\frac{p+q}{2}\pi\right) \right) \\ & \times \cos p\beta. \end{aligned} \quad (74)$$

If  $p + q$  is an even number, all integrals are zero.

*Proof.* Regarding the first case, trigonometric identities decompose the latter part as

$$\begin{aligned} & \cos q\omega \cos(p\omega - p\beta) \\ &= \frac{1}{2} ((\cos(p+q)\omega + \cos(p-q)\omega) \cos p\beta \\ & + (\sin(p+q)\omega + \sin(p-q)\omega) \sin p\beta). \end{aligned}$$

This leads to

$$\begin{aligned} & \frac{1}{2} \int_0^{2\pi} \sin(pnA \cos \omega) ((\cos(p+q)\omega + \cos(p-q)\omega) \cos p\beta \\ & + (\sin(p+q)\omega + \sin(p-q)\omega) \sin p\beta) d\omega \\ &= \frac{1}{4} \int_0^{2\pi} (\sin((p+q)\omega + \rho nA \cos \omega) \\ & + \sin(-(p+q)\omega + \rho nA \cos \omega)) d\omega \cos p\beta \\ & + \frac{1}{4} \int_0^{2\pi} (\sin((p-q)\omega + \rho nA \cos \omega) \\ & + \sin(-(p-q)\omega + \rho nA \cos \omega)) d\omega \cos p\beta \\ & + \frac{1}{4} \int_0^{2\pi} (-\cos((p+q)\omega + \rho nA \cos \omega) \\ & + \cos(-(p+q)\omega + \rho nA \cos \omega)) d\omega \sin p\beta \\ & + \frac{1}{4} \int_0^{2\pi} (-\cos((p-q)\omega + \rho nA \cos \omega) \\ & + \cos(-(p-q)\omega + \rho nA \cos \omega)) d\omega \sin p\beta. \end{aligned}$$

Set a new parameter  $w = \omega - \pi/2$ . The function inside of integral is periodic by  $2\pi$ , i.e. the interval can be shifted by  $[-\pi, \pi]$ . The first term is

$$\begin{aligned} & \frac{1}{4} \int_{-\pi}^{\pi} \left( \sin\left((p+q)w + \frac{p+q}{2}\pi + \rho nA \cos\left(w + \frac{\pi}{2}\right)\right) \right. \\ & \left. + \sin\left(-(p+q)w - \frac{p+q}{2}\pi + \rho nA \cos\left(w + \frac{\pi}{2}\right)\right) \right) dw \cos p\beta \\ &= \frac{\pi}{2} (J_{(p+q)}(\rho nA) - J_{-(p+q)}(\rho nA)) \sin\left(\frac{p+q}{2}\pi\right) \cos p\beta \\ &= \frac{\pi}{2} (1 - (-1)^{(p+q)}) J_{(p+q)}(\rho nA) \sin\left(\frac{p+q}{2}\pi\right) \cos p\beta, \end{aligned}$$

by  $J_{\nu}(z) = (-1)^{\nu} J_{-\nu}(z)$  for integer  $\nu$ . By a similar manner, the second term is

$$\begin{aligned} & \frac{1}{4} \int_{-\pi}^{\pi} \left( \sin\left((p-q)w + \frac{p-q}{2}\pi + \rho nA \cos\left(w + \frac{\pi}{2}\right)\right) \right. \\ & \left. + \sin\left(-(p-q)w - \frac{p-q}{2}\pi + \rho nA \cos\left(w + \frac{\pi}{2}\right)\right) \right) dw \cos p\beta \\ &= \frac{\pi}{2} (1 - (-1)^{(p-q)}) J_{(p-q)}(\rho nA) \sin\left(\frac{p-q}{2}\pi\right) \cos p\beta. \end{aligned}$$

For cosine parts,

$$\begin{aligned} & \frac{1}{4} \int_{-\pi}^{\pi} \left( -\cos\left((p+q)w + \frac{p+q}{2}\pi + \rho nA \cos\left(w + \frac{\pi}{2}\right)\right) \right. \\ & \left. + \cos\left(-(p+q)w - \frac{p+q}{2}\pi + \rho nA \cos\left(w + \frac{\pi}{2}\right)\right) \right) dw \sin p\beta \\ &= \frac{\pi}{2} (-1 + (-1)^{(p+q)}) J_{(p+q)}(\rho nA) \cos\left(\frac{p+q}{2}\pi\right) \sin p\beta. \end{aligned}$$

This is because the sine term with integral is canceled by the integral. In a similar manner, the second term is

$$\begin{aligned} & \frac{1}{4} \int_{-\pi}^{\pi} \left( -\cos\left((p-q)w + \frac{p-q}{2}\pi + \rho nA \cos\left(w + \frac{\pi}{2}\right)\right) \right. \\ & \left. + \cos\left(-(p-q)w - \frac{p-q}{2}\pi + \rho nA \cos\left(w + \frac{\pi}{2}\right)\right) \right) dw \sin p\beta \\ &= \frac{\pi}{2} (-1 + (-1)^{(p-q)}) J_{(p-q)}(\rho nA) \cos\left(\frac{p-q}{2}\pi\right) \sin p\beta. \end{aligned}$$

By adding up and  $(-1)^{p+q} = (-1)^{p-q}$  for integer  $p$  and  $q$ , the total value is

$$\begin{aligned} & \int_0^{2\pi} \sin(pnA \cos \omega) \cos q\omega \cos(p\omega - p\beta) d\omega \\ &= \frac{\pi}{2} (1 - (-1)^{(p+q)}) \left( J_{(p+q)}(\rho nA) \sin\left(\frac{p+q}{2}\pi\right) \right. \\ & \left. + J_{(p-q)}(\rho nA) \sin\left(\frac{p-q}{2}\pi\right) \right) \cos p\beta \\ & + \frac{\pi}{2} (-1 + (-1)^{(p+q)}) \left( J_{(p+q)}(\rho nA) \cos\left(\frac{p+q}{2}\pi\right) \right. \\ & \left. + J_{(p-q)}(\rho nA) \cos\left(\frac{p-q}{2}\pi\right) \right) \sin p\beta \\ &= \begin{cases} \Lambda, & p+q \text{ is odd,} \\ 0, & p+q \text{ is even,} \end{cases} \end{aligned}$$

where

$$\begin{aligned} \Lambda &= \pi \left( J_{(p+q)}(\rho nA) \sin\left(\frac{p+q}{2}\pi\right) \right. \\ & \left. + J_{(p-q)}(\rho nA) \sin\left(\frac{p-q}{2}\pi\right) \right) \cos p\beta. \end{aligned}$$

The other results are obtained in a similar manner.  $\square$

The Lemma 1 is a special case of  $p = 2m$  and  $q = 1$  with a Bessel identity of  $J_{\nu+1}(z) = \frac{2\nu}{z} J_{\nu}(z) - J_{\nu-1}(z)$  for  $\nu \in \mathbb{Z}$ . By a similar way, a generalized corollary can be drawn as follows.

**Corollary 4.** Consider generalized averaging integrals over a period of the motion for integers  $p$  and  $q$ . If  $p + q$  is an even number, the averaging integrals are given by

$$\int_0^{2\pi} \cos(\rho n A \cos \omega) \cos q \omega \cos(p\omega - p\beta) d\omega$$

$$= \pi \left( J_{(p-q)}(\rho n A) \cos\left(\frac{p-q}{2}\pi\right) + J_{(p+q)}(\rho n A) \cos\left(\frac{p+q}{2}\pi\right) \right)$$

$$\times \cos p\beta, \quad (75)$$

$$\int_0^{2\pi} \cos(\rho n A \cos \omega) \sin q \omega \cos(p\omega - p\beta) d\omega$$

$$= \pi \left( J_{(p-q)}(\rho n A) \cos\left(\frac{p-q}{2}\pi\right) - J_{(p+q)}(\rho n A) \cos\left(\frac{p+q}{2}\pi\right) \right)$$

$$\times \sin p\beta, \quad (76)$$

$$\int_0^{2\pi} \cos(\rho n A \cos \omega) \cos q \omega \sin(p\omega - p\beta) d\omega$$

$$= \pi \left( -J_{(p-q)}(\rho n A) \cos\left(\frac{p-q}{2}\pi\right) - J_{(p+q)}(\rho n A) \cos\left(\frac{p+q}{2}\pi\right) \right)$$

$$\times \sin p\beta, \quad (77)$$

$$\int_0^{2\pi} \cos(\rho n A \cos \omega) \sin q \omega \sin(p\omega - p\beta) d\omega$$

$$= \pi \left( J_{(p-q)}(\rho n A) \cos\left(\frac{p-q}{2}\pi\right) - J_{(p+q)}(\rho n A) \cos\left(\frac{p+q}{2}\pi\right) \right)$$

$$\times \cos p\beta. \quad (78)$$

If  $p + q$  is an odd number, the integrals are all zero.

#### APPENDIX B DERIVATION OF SLOW FLOW MODEL

Before applying the solvability condition of (20), the derivative term is rewritten as

$$D_1 D_0 x_0 = -\frac{\partial A(T_1)}{\partial T_1} \sigma \sin \omega - \frac{\partial \beta(T_1)}{\partial T_1} \sigma A(T_1) \cos \omega.$$

By Lemma 1 and Corollary 2, the real part is reduced as

$$0 = \int_0^{2\pi} \left[ 2A\mu(A)\sigma \sin \omega \cos \omega + (\sigma^2 - 1) A \cos^2 \omega - K_3 A^3 \cos^4 \omega \right.$$

$$- K_5 A^5 \cos^6 \omega - K_7 A^7 \cos^8 \omega + U^2 a_u(0) \sum_{n=1}^N b(n) \sin(\rho n A \cos \omega) \cos \omega$$

$$+ 2U^2 \sum_{n=1}^N \sum_{m=1}^M b(n) a_u(m) \sin(\rho n A \cos \omega) \cos \omega \cos(2m(\omega - \beta))$$

$$+ 2U^2 \sum_{n=1}^N \sum_{m=1}^M b(n) b_u(m) \sin(\rho n A \cos \omega) \cos \omega \sin(2m(\omega - \beta))$$

$$+ 2 \left( \frac{\partial A}{\partial T_1} \right) \sigma \sin \omega \cos \omega + 2 \left( \frac{\partial \beta}{\partial T_1} \right) A \sigma \cos^2 \omega \Big] d\omega$$

$$= -2\pi \frac{3K_3 A^3}{8} - 2\pi \frac{5K_5 A^5}{16} - 2\pi \frac{35K_7 A^7}{128}$$

$$+ 2\pi \sigma A \frac{\partial \beta}{\partial T_1} + \frac{2\pi(\sigma^2 - 1)A}{2} + 2\pi U^2 a_u(0) \left( \sum_{n=1}^N b(n) J_1(\rho n A) \right)$$

$$+ 2\pi U^2 \sum_{n=1}^N \sum_{m=1}^M (-1)^m b(n) a_u(m)$$

$$\times (J_{2m+1}(\rho n A) - J_{2m-1}(\rho n A)) \cos(2m\beta)$$

$$+ 2\pi U^2 \sum_{n=1}^N \sum_{m=1}^M (-1)^m b(n) b_u(m)$$

$$\times (-J_{2m+1}(\rho n A) + J_{2m-1}(\rho n A)) \sin(2m\beta),$$

and the imaginary part is then

$$0 = \int_0^{2\pi} \left[ 2A\mu(A)\sigma \sin^2 \omega + (\sigma^2 - 1) A \cos \omega \sin \omega \right.$$

$$- K_3 A^3 \cos^3 \omega \sin \omega - K_5 A^5 \cos^5 \omega \sin \omega - K_7 A^7 \cos^7 \omega \sin \omega$$

$$+ U^2 a_u(0) \sum_{n=1}^N b(n) \sin(\rho n A \cos \omega) \sin \omega$$

$$+ 2U^2 \sum_{n=1}^N \sum_{m=1}^M b(n) a_u(m) \sin(\rho n A \cos \omega) \sin \omega \cos(2m(\omega - \beta))$$

$$+ 2U^2 \sum_{n=1}^N \sum_{m=1}^M b(n) b_u(m) \sin(\rho n A \cos \omega) \sin \omega \sin(2m(\omega - \beta))$$

$$+ 2 \left( \frac{\partial A}{\partial T_1} \right) \sigma \sin^2 \omega + 2 \left( \frac{\partial \beta}{\partial T_1} \right) A \sigma \cos \omega \sin \omega \Big] d\omega$$

$$= 2\pi \sigma A \mu(A) + 2\pi \sigma \left( \frac{\partial A}{\partial T_1} \right)$$

$$+ 2\pi U^2 \sum_{n=1}^N \sum_{m=1}^M (-1)^m b(n) a_u(m)$$

$$\times (-J_{2m+1}(\rho n A) - J_{2m-1}(\rho n A)) \sin(2m\beta)$$

$$+ 2\pi U^2 \sum_{n=1}^N \sum_{m=1}^M (-1)^m b(n) b_u(m)$$

$$\times (-J_{2m+1}(\rho n A) - J_{2m-1}(\rho n A)) \cos(2m\beta).$$

Equations in real and imaginary part lead to two partial differential equations as

$$\frac{\partial A}{\partial T_1} = -A\mu(A) - \frac{U^2}{\sigma} \sum_{n=1}^N \sum_{m=1}^M (-1)^{m+1} b(n) a_u(m)$$

$$\times (J_{2m+1}(\rho n A) + J_{2m-1}(\rho n A)) \sin(2m\beta)$$

$$- \frac{U^2}{\sigma} \sum_{n=1}^N \sum_{m=1}^M (-1)^{m+1} b(n) b_u(m)$$

$$\times (J_{2m+1}(\rho n A) + J_{2m-1}(\rho n A)) \cos(2m\beta), \quad (79)$$

$$A \frac{\partial \beta}{\partial T_1} = \frac{3K_3 A^3}{8\sigma} + \frac{5K_5 A^5}{16\sigma} + \frac{35K_7 A^7}{128\sigma} - \frac{(\sigma^2 - 1)A}{2\sigma}$$

$$- \frac{U^2 a_u(0)}{\sigma} \left( \sum_{n=1}^N b(n) J_1(\rho n A) \right)$$

$$- \frac{U^2}{\sigma} \sum_{n=1}^N \sum_{m=1}^M (-1)^{m+1} b(n) a_u(m)$$

$$\times (-J_{2m+1}(\rho n A) + J_{2m-1}(\rho n A)) \cos(2m\beta)$$

$$- \frac{U^2}{\sigma} \sum_{n=1}^N \sum_{m=1}^M (-1)^{m+1} b(n) b_u(m)$$

$$\times (J_{2m+1}(\rho n A) - J_{2m-1}(\rho n A)) \sin(2m\beta). \quad (80)$$

The result in [26] is a special case with  $a_u(0) = 1$ ,  $a_u(1) = 1/2$ , and zeros for the other Fourier coefficients of the input waveform. By assuming  $A > 0$ , rewriting summations in a matrix form, and using the ordinary differential operator, (79) and (80) yield (29) and (30).

#### ACKNOWLEDGMENT

The authors would like to thank David Brunner and Richard Schroedter of ACIN in TU Wien for fruitful discussions.

## REFERENCES

- [1] A. D. Yalcinkaya, H. Urey, D. Brown, T. Montague, and R. Sprague, "Two-axis electromagnetic microscanner for high resolution displays," *J. Microelectromech. Syst.*, vol. 15, no. 4, pp. 786–794, 2006.
- [2] S. T. S. Holmström, U. Baran, and H. Urey, "MEMS laser scanners: A review," *J. Microelectromech. Syst.*, vol. 23, no. 2, pp. 259–275, 2014.
- [3] X. Duan, H. Li, X. Li, K. R. Oldham, and T. D. Wang, "Axial beam scanning in multiphoton microscopy with MEMS-based actuator," *Opt. Express*, vol. 25, no. 3, pp. 2195–2205, Feb. 2017.
- [4] S. Bakas, D. Uttamchandani, and R. Bauer, "Light-sheet microscopy using MEMS and active optics for 3D image acquisition control," in *MOEMS and Miniaturized Systems XIX*, vol. 11293. SPIE, 2020, p. 112930M.
- [5] U. Hofmann, M. Aikio, J. Janes, F. Senger, V. Stenchly, J. Hagge, H.-J. Quenzer, M. Weiss, T. v. Wantoch, C. Mallas, B. Wagner, and W. Benecke, "Resonant biaxial 7-mm MEMS mirror for omnidirectional scanning," *J. Micro/Nanolith. MEMS MOEMS*, vol. 13, no. 1, p. 011103, Dec. 2013.
- [6] K. Ito, C. Niclass, I. Aoyagi, H. Matsubara, M. Soga, S. Kato, M. Maeda, and M. Kagami, "System design and performance characterization of a mems-based laser scanning time-of-flight sensor based on a 256x64-pixel single-photon imager," *IEEE Photonics J.*, vol. 5, p. 6800114, 2013.
- [7] N. Druml, I. Maksymova, T. Thurner, D. van Lierop, M. Hennecke, and A. Foroutan, "1D MEMS Micro-Scanning LiDAR," in *Int. Conf. on Sensor Device Technologies and Appl.*, 2018.
- [8] T. Sandner, T. Grasshoff, M. Wildenhain, and M. Schwarzenberg, "Hybrid assembled MEMS scanner array with large aperture for fast scanning LIDAR systems," *tm - Technisches Messen*, vol. 86, no. 3, pp. 151–163, 2019.
- [9] F. Schwarz, F. Senger, J. Albers, P. Malaurie, C. Janicke, L. Pohl, F. Heinrich, D. Kaden, H.-J. Quenzer, F. Lofink, A. Bahr, T. v. Wantoch, and U. Hofmann, "Resonant 1D MEMS mirror with a total optical scan angle of 180° for automotive LiDAR," in *MOEMS and Miniaturized Systems XIX*, vol. 11293. SPIE, Feb. 2020, p. 1129309.
- [10] K. L. Turner, S. A. Miller, P. G. Hartwell, N. C. MacDonald, S. H. Strogatz, and S. G. Adams, "Five parametric resonances in a microelectromechanical system," *Nature*, vol. 396, no. 6707, pp. 149–152, Nov. 1998.
- [11] J. F. Rhoads, S. W. Shaw, K. L. Turner, J. Moehlis, B. E. DeMartini, and W. Zhang, "Generalized parametric resonance in electrostatically actuated microelectromechanical oscillators," *J. Sound Vib.*, vol. 296, no. 4, pp. 797–829, 2006.
- [12] A. H. Nayfeh and N. E. Sanchez, "Bifurcations in a forced softening duffing oscillator," *International Journal of Non-Linear Mechanics*, vol. 24, no. 6, pp. 483–497, 1989.
- [13] C. Ataman and H. Urey, "Modeling and characterization of comb-actuated resonant microscanners," *J. Micromech. Microeng.*, vol. 16, no. 1, p. 9, 2006.
- [14] D. Brunner, H. W. Yoo, T. Thurner, and G. Schitter, "Data based modelling and identification of nonlinear SDOF MOEMS mirror," in *Proc. SPIE 10931*, 2019, p. 1093117.
- [15] H. W. Yoo, N. Druml, D. Brunner, C. Schwarzl, T. Thurner, M. Hennecke, and G. Schitter, "MEMS-based lidar for autonomous driving," *Elektrotechnik und Informationstechnik*, vol. 135, no. 6, pp. 408–418, 2018.
- [16] W. Zhang, R. Baskaran, and K. L. Turner, "Effect of cubic nonlinearity on auto-parametrically amplified resonant MEMS mass sensor," *Sensor. Actuat. A-Phys.*, vol. 102, no. 1, pp. 139–150, Dec. 2002.
- [17] W. Zhang and K. L. Turner, "Application of parametric resonance amplification in a single-crystal silicon micro-oscillator based mass sensor," *Sensor. Actuat. A-Phys.*, vol. 122, no. 1, pp. 23–30, Jul. 2005.
- [18] C. Ataman, H. Urey, and A. Wolter, "A Fourier transform spectrometer using resonant vertical comb actuators," *J. Micromech. Microeng.*, vol. 16, no. 12, pp. 2517–2523, 2006.
- [19] A. Frangi, A. Guerrieri, R. Carminati, and G. Mendicino, "Parametric Resonance in Electrostatically Actuated Micromirrors," *IEEE Trans. Ind. Electron.*, vol. 64, no. 2, pp. 1544–1551, Feb. 2017.
- [20] K. B. Lee, "Non-contact electrostatic microactuator using slit structures: theory and a preliminary test," *J. Micromech. Microeng.*, vol. 17, no. 11, pp. 2186–2196, 2007.
- [21] Y. Linzon, B. Ilic, S. Lulinsky, and S. Krylov, "Efficient parametric excitation of silicon-on-insulator microcantilever beams by fringing electrostatic fields," *J. of Appl. Phys.*, vol. 113, no. 16, p. 163508, 2013.
- [22] H. W. Yoo and G. Schitter, "Complex valued state space model for weakly nonlinear Duffing oscillator with noncollocated external disturbance," in *21st IFAC World Congress*, Jul. 2020, p. in press.
- [23] T. Izawa, T. Sasaki, and K. Hane, "Scanning micro-mirror with an electrostatic spring for compensation of hard-spring nonlinearity," *Micromachines*, vol. 8, no. 8, p. 240, 2017.
- [24] W. Shahid, Z. Qiu, X. Duan, H. Li, T. D. Wang, and K. R. Oldham, "Modeling and Simulation of a Parametrically Resonant Micromirror With Duty-Cycled Excitation," *J. Microelectromech. Syst.*, vol. 23(6): 1440–1453, 2014.
- [25] H. Li, P. Barnes, E. Harding, X. Duan, T. D. Wang, and K. R. Oldham, "Large-Displacement Vertical Electrostatic Microactuator Dynamics Using Duty-Cycled Softening/Stiffening Parametric Resonance," *J. Microelectromech. Syst.*, vol. 28, no. 3, pp. 351–361, 2019.
- [26] H. W. Yoo, S. Albert, and G. Schitter, "Accurate analytic model of a parametrically driven resonant MEMS mirror with a Fourier series based torque approximation," *J. Microelectromech. Syst.*, vol. 5, no. 29, pp. 1431–1442, 2020.
- [27] A. Wolter, S.-T. Hsu, H. Schenk, and H. K. Lakner, "Applications and requirements for MEMS scanner mirrors," in *Proc. SPIE 5719*, Jan. 2005, pp. 64–76.
- [28] "LV 124: Electric and electronic components in motor vehicles up to 3.5 t - general requirements, test conditions and tests (VW 80000)," Volkswagen, Tech. Rep. 8MA00, 2013.
- [29] A. Strasser, P. Stelzer, C. Steger, and N. Druml, "Speed-Up of MEMS Mirror's Transient Start-Up Procedure," in *2019 IEEE Sensors Applications Symposium (SAS)*, 2019, pp. 1–5.
- [30] D. Brunner, H. W. Yoo, and G. Schitter, "Precise phase control of resonant moems mirrors by comb-drive current feedback," *Mechatronics*, vol. 71, p. 102420, 2020.
- [31] H. Schenk, P. Durr, T. Haase, D. Kunze, U. Sobe, H. Lakner, and H. Kuck, "Large deflection micromechanical scanning mirrors for linear scans and pattern generation," *IEEE Journal of Selected Topics in Quantum Electronics*, vol. 6, no. 5, pp. 715–722, 2000.
- [32] B. Edamana, B. Hahn, J. S. Pulskamp, R. G. Polcawich, and K. Oldham, "Modeling and Optimal Low-Power On-Off Control of Thin-Film Piezoelectric Rotational Actuators," *IEEE/ASME Transactions on Mechatronics*, vol. 16, no. 5, pp. 884–896, 2011.
- [33] S. Maruyama, M. Nakada, M. Mita, T. Takahashi, H. Fujita, and H. Toshiyoshi, "An Equivalent Circuit Model for Vertical Comb Drive MEMS Optical Scanner Controlled by Pulse Width Modulation," *IEEE Trans. on Sensor and Micromachines*, vol. 132, no. 1, pp. 1–9, 2012.
- [34] I. Maksymova, P. Greiner, L. C. Niedermueller, and N. Druml, "Detection and Compensation of Periodic Jitters of Oscillating MEMS Mirrors used in Automotive Driving Assistance Systems," in *2019 IEEE Sensors Applications Symposium (SAS)*, 2019, pp. 1–5.
- [35] D. Brunner, H. W. Yoo, and G. Schitter, "Linear modeling and control of comb-actuated resonant MEMS mirror with nonlinear dynamics," *IEEE Trans. Ind. Electron.*, vol. 67, no. -, p. In press, 2020.
- [36] D. M. Levy and J. B. Keller, "Instability intervals of Hill's equation," *Communications on Pure and Applied Mathematics*, vol. 16, no. 4, pp. 469–476, 1963.
- [37] A. H. Nayfeh, "Characteristic Exponents and Stability of Hill's Equation," *J. Appl. Mech.*, vol. 39, no. 4, pp. 1156–1158, 1972.
- [38] P. Pedersen, "On stability diagrams for damped Hill equations," *Quart. Appl. Math.*, vol. 42, no. 4, pp. 477–495, 1985.
- [39] C. Cattani, E. A. Grebenikov, and A. N. Prokopenya, "On stability of the Hill equation with damping," *Nonlinear Oscill.*, vol. 7, no. 2, pp. 168–178, Apr. 2004.
- [40] I. Kovacic, R. Rand, and S. Mohamed Sah, "Mathieu's Equation and Its Generalizations: Overview of Stability Charts and Their Features," *Appl. Mech. Rev.*, vol. 70, no. 2, p. 020802, Mar. 2018.
- [41] H. W. Yoo, R. Riegler, D. Brunner, S. Albert, T. Thurner, and G. Schitter, "Vibration influence evaluation of MEMS scanning system for automotive lidar," *arXiv:2010.08327 [eess.SY]*, 2020.
- [42] H. W. L. A. M. van Lierop, M. A. G. Suijlen, and M. J. van Os, "MEMS scanning micromirror," US Patent 9,588,337 B2, Mar., 2017.
- [43] E. Esmailzadeh, D. Younesian, and H. Askari, *Analytical Methods in Nonlinear Oscillations*. Springer Netherlands, 2019.
- [44] H. W. Yoo, D. Brunner, T. Thurner, and G. Schitter, "MEMS test bench and its uncertainty analysis for evaluation of MEMS mirrors," in *8th IFAC Symp. on Mechatronic Syst.*, Sep. 2019, pp. 49–54.
- [45] A. H. Nayfeh, *Introduction to perturbation techniques*. Wiley, New York, 1981.
- [46] J. Han, L. Li, G. Jin, J. Feng, B. Li, H. Jia, and W. Ma, "Vibration Identification of Folded-MEMS Comb Drive Resonators," *Micromachines*, vol. 9, no. 8, p. 381, 2018.



- [47] J.-H. He, "Bookkeeping Parameter in Perturbation Methods," *Int. J. Nonlin. Sci. Num.*, vol. 2, no. 3, pp. 257–264, Sep. 2001.
- [48] A. M. Elshurafa, K. Khirallah, H. H. Tawfik, A. Emira, A. K. S. A. Aziz, and S. M. Sedky, "Nonlinear dynamics of spring softening and hardening in folded-MEMS comb drive resonators," *J. Microelectromech. Syst.*, vol. 20, no. 4, pp. 943–958, 2011.
- [49] K. Yagasaki, M. Sakata, and K. Kimura, "Dynamics of a weakly nonlinear system subjected to combined parametric and external excitation," *J. Appl. Mech.*, vol. 57, no. 1, pp. 209–217, 1990.
- [50] G. Biagetti, P. Crippa, L. Falaschetti, and C. Turchetti, "Discrete Bessel functions for representing the class of finite duration decaying sequences," in *2016 24th European Signal Processing Conference (EUSIPCO)*, Aug. 2016, pp. 2126–2130.
- [51] D. Brunner, H. W. Yoo, and G. Schitter, "Digital asynchronous phase locked loop for precision control of MOEMS scanning mirror," in *8th IFAC Symp. on Mechatronic Syst.*, Sep. 2019, pp. 43–48.
- [52] J. Guckenheimer and P. J. Holmes, *Nonlinear Oscillations, Dynamical Systems, and Bifurcations of Vector Fields*. Springer-Verlag New York, 1983.
- [53] B. E. DeMartini, J. F. Rhoads, K. L. Turner, S. W. Shaw, and J. Moehlis, "Linear and Nonlinear Tuning of Parametrically Excited MEMS Oscillators," *J. Microelectromech. Syst.*, vol. 16, no. 2, pp. 310–318, Apr. 2007.



**Han Woong Yoo** (Member, IEEE) received the B.S. degree from Yonsei University, the M.S. degree in electrical engineering from Seoul National University in 2007, and the Ph.D. degree in optomechanics and adaptive optics for confocal microscopy from the Delft University of Technology in 2015. He worked at the Samsung Advanced Institute of Technology (SAIT) and Samsung Electronics Company Ltd., semi-conductor business, for low-power digital RF and algorithms for reliability of multi-level nonvolatile memories. He is currently a Post-

Doctoral Researcher in advanced mechatronic systems with the Automation and Control Institute (ACIN), TU Wien. His main research interests include optical metrology, precision mechatronics systems, and biomedical imaging.



**Stephan Albert** received the M.A. degree as a Fulbright Scholar from Stony Brook University in 2007, the Diploma degree from TU Munich in 2010, and the Ph.D. degree in physics from TU Munich in 2015. He is currently a Principal Engineer of MEMS devices with Infineon Technologies AG, Neubiberg, Germany. He has worked experimentally in the fields of quantum optics, ultracold atoms, and magnetism and theoretically in the field of many-body physics. At Infineon, he is responsible for the design, modeling, and the development of integration concepts

for MEMS devices, such as pressure sensors, accelerometers, and scanning mirror devices.



**Georg Schitter** (Senior Member, IEEE) received the M.Sc. degree in electrical engineering from TU Graz, Austria, in 2000, and the M.Sc. and Ph.D. degrees from ETH Zürich, Switzerland, in 2004. He is currently a Professor of advanced mechatronic systems with the Automation and Control Institute (ACIN), TU Wien. His primary research interests include high-performance mechatronic systems, particularly for applications in the high-tech industry, scientific instrumentation, and mechatronic imaging systems, such as AFM, scanning laser and LIDAR

systems, telescope systems, adaptive optics, and lithography systems for semiconductor industry. He received the Paper Best Award of IEEE/ASME Transactions on Mechatronics in 2017, the IFAC Mechatronics from 2008 to 2010, and the Asian Journal of Control from 2004 to 2005 and the 2013 IFAC Mechatronics Young Researcher Award. He has served as an Associate Editor for IFAC Mechatronics, Control Engineering Practice, and the IEEE Transactions on Mechatronics.